The Atmospheric Surface Layer over Dronning Maud Land, Antarctica

Gabin H. Urbancic
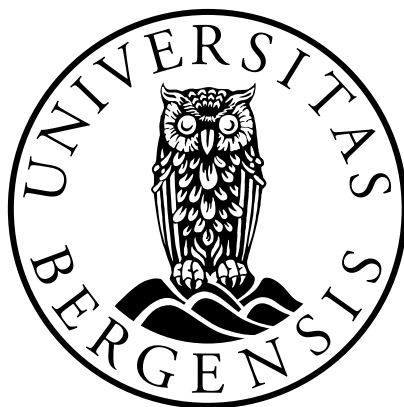
Acknowledgements

I would like to primarily thank my supervisor Joachim Reuder, for the guidance, patience, and for giving me the freedom to explore the field in a less-than-optimal way.

Big thanks to Timo Vihma and Irene Suomi from FMI for their advice and significant contributions to this work. Without them, this thesis would of been closer to a piece of contemporary poetry than a work of science.

Kippis, to the whole FINNARP2018 expedition, and specifically my scientific team, Juho Vehviläinen and Kati Anttila.

Last but not least, thank you to my colleagues at GFI who helped develop the ideas of this work, one beer at a time; Stephan, Andrew, Omar, Pablo, Kjersti, the list goes on...

FINNARP2018, ABOA, Dronning Maud Land, Antarctica

Photo by Priit Tisler.

Abstract

The Atmospheric Surface Layer (ASL), over Dronning Maud Land, is investigated for the mean meteorological conditions, the structure of turbulence, and the phenomenology of the area. The data set is the accumulation of data from three separate expeditions to Aboa station, Dronning Maud Land. The expeditions were during the austral summer of 2010-2011, 2014-2015, and 2018-2019. The site of study, known as AWS5, is 10 km to the south-east of Aboa station and is on a gently sloping glacier. CSAT3 sonic anemometers were installed at 2 m and 10 m.

The ASL at AWS5 is driven by both the synoptic pressure gradient and the katabatic force. For the area of study, the two are aligned resulting in very high wind constancy. Katabatic flows occur during the early morning, when the solar zenith angle is too large to warm the surface, resulting in surface-based inversions. The wind maxima is often below 10 m and the 2 m wind speed reaches 3 m/s. As the observations are over a gentle slope, the kinematic heat flux is the dominant parameter of turbulence in the ASL, resulting in a maximum attainable stability parameter. As a wealth of phenomena occur during stable conditions, the Eularian autocorrelation function (EAF) was used to examine oscillations and hence wind meandering. The loop-parameter (m) was found to separate the intervals into periods with waves and periods without waves. Using this criteria to remove periods with wave activity, the scatter observed in ϕ_M and ϕ_H was reduced. This serves as a good proof-of-concept for using m to understand the influence of waves on MOST.

Contents

Chapter 1

Introduction and Background

1.1 Introduction

The atmospheric boundary layer (ABL) is the lowest part of the atmosphere, where the conditions respond to changes at the surface in the timescale of hours. The importance of the ABL is two fold. Firstly, it is the behaviour of the ABL which dictates the interaction between the atmosphere and other constituents of the earth system. Secondly, human activity is almost entirely in the ABL and can be highly influenced by its meteorological conditions. The atmospheric surface layer (ASL) is the lowest part of the ABL, and is in direct contact with earths surface. In the ASL, the structure of turbulence and the profiles of mean wind speed and temperature are dependent on the surface conditions, and not the flow aloft. In quasi-stationary and horizontally homogeneous conditions, the ASL is well described by similarity theory (Högström, 1996). It is this similarity theory which commonly serves as the lower boundary condition while modelling atmospheric flows. The ABL under stable conditions is often non-stationary and the similarity theory is not formally valid. This causes difficulty in modelling and forecasting the stable ABL (Holtslag et al., 2013; Fernando and Weil, 2010). Under stable conditions, surface fluxes are overestimated resulting in a warm bias in numerical weather prediction (NWP) models (Cuxart et al., 2006; Atlaskin and Vihma, 2012). As stable conditions are prominent in polar regions, misrepresentation of the surface conditions can complicate the ability to understand the changing polar climate (Boe et al., 2009; Esau and Zilitinkevich, 2010; Vihma et al., 2014)

Stable stratification in the ABL can be generated by radiative cooling of the surface, as well as through warm-air advection over colder surfaces (Smedman et al., 1993). It inhibits turbulent fluxes and by consequence, the upward communication of the surface conditions. By definition, this implies a reduction in the height of the ABL. In polar regions, due to the strong radiative cooling at the surface, the ABL can have a depth as small as 10 m. In such cases, the ASL is shallow to the point where it is no longer practical to consider.

With increasing stability, through radiative cooling, a critical point is reached where the surface and air-aloft are completely decoupled. This follows the collapse of turbulence that occurs under strongly stratified conditions (Flores and Riley, 2011; van de Wiel et al., 2007). In such a regime, the turbulence generated at the surface no longer acts as a frictional force on the atmosphere, resulting in its free evolution. The horizontal pressure gradients accelerates the flow and the flow becomes unstable. The turbulence associated with its instability partially erodes the inversion through mixing, decreasing the stability, and re-coupling the

atmosphere to the surface. Radiative cooling starts increasing the stability again resulting in a periodic evolution (Van de Wiel et al., 2002b,a, 2003). During periods of strong stratification, the ABL exists in a continuously evolving state.

Further complications arise in stable conditions as a wealth of phenomena can occur; including drainage flows, solitary waves, gravity waves and microfronts (Mahrt et al., 2015). They are referred to as meso- or submeso-scale motions. These motions, superimposed on the mean flow, complicate the structure of turbulence. When scales of the waves are similar to the scales of turbulence, energy exchange can occur between them resulting in additional complexity (Sun et al., 2014, 2015). The occurrence of meso- and submeso- motions is highly variable and is depend on both location and the mean conditions. As such, a universal climatology for submeso- and meso-scale motions in the ABL is not possible.

Both the periodic evolution of stably stratified ABL and submeso-scale motions contribute to variability in the turbulent intensity. Such variability falls under the umbrella of what is called intermittent turbulence (Mahrt, 1989, 1998; Sun et al., 2002; Van de Wiel et al., 2002b; Sun et al., 2004). Intermittent turbulence is therefore also tied to variations in the mean wind speed, wind direction, and temperature. Variability in the mean conditions is often considered under the framework of wind meandering (Anfossi et al., 2005; Mahrt, 2007; Mortarini et al., 2013). Both wind meandering and intermittent turbulence describe the unsteady nature of atmospheric flows. As such, they are both possible candidates for developing improved parameterizations of turbulence under stable conditions.

Studying the ABL over Antarctica is challenging due to the lack of available observations. This lack of data is due to the logistical difficulty of operating in polar regions (Kral et al., 2018). Furthermore, eddy-covariance data requires manned staff to maintain, restricting the attainability of new data sets. The disparity of observations in Antarctica in comparison to mid-latitudes results in a bias towards mid-latitude conditions in models. The negative surface energy budget of Antarctica, due to high albedo and large solar zenith angles, results in a propensity for very stable conditions. As very stable conditions are inherently unsteady, standard similarity theory is invalid. Model misrepresentation of ABL during stable conditions is therefore problematic for modelling the polar atmosphere (Holtslag et al., 2013; Vihma et al., 2014).

The following work is a first look into the ASL in the vicinity of Aboa station, Dronning Maud Land. Multiple topics are discussed which cover general and particular properties of the ASL. It was the ambition of this thesis to introduce a new eddy-covariance data set from the Antarctic continent, as well as to find interesting features in the data to motivate future work. As such, more problems are introduced than answers. Chapter 2 introduces the data set and describes the data processing and eddy-covariance methods. Chapter 3 introduces the area of study and presents the mean meteorological conditions. Chapter 4 investigates the phenomenology of the area with emphasis on oscillatory and katabatic flows. Chapter 5 considers the structure of turbulence in the ASL through the understanding developed in the previous chapters. Lastly, Chapter 6 summarizes the results.

1.2   Understanding the Atmospheric Surface Layer

This section is an introduction to the ASL starting from the logarithmic profile. Motivated by aerodynamics, the logarithmic profile (LP) was first derived in the study of flows over a smooth surface (Anderson Jr., 2005). This discovery led to the modern understanding of boundary layers, as well as where -boundary layer- received its name. It was shortly after the success of the theory resulting in the LP, that meteorologist began attempting a similar theory for the atmospheric boundary layer (Monin and Obukhov, 1954). The following derivation is based off Kundu and Cohen (2002).

The correct boundary condition for a flow over a smooth surface was determined to be not a free-slip, as initially believed, but a no-slip condition. A no-slip boundary condition implies that even though viscosity can be neglected away from the boundaries, there is a small layer near a surface, for all Reynolds number (Re), where viscosity is important. This holds even in the $Re \rightarrow \infty$ limit. To determine the velocity profile, the method of matched asymptotics is applied. In a steady flow over a flat surface, the total stress (τ) is

$$\tau = \rho\nu(dU/dz) - \rho\overline{u'w'}, \tag{1.1}$$

where ρ is the density, U is the horizontal velocity, z is the height over the surface, ν is the viscosity, and $\overline{u'w'}$ is the Reynolds stress. Near the surface, in what is called the inner-region, the velocity profile is assumed independent of the free-flow velocity. The physical parameters of the problem are U, z, ν and the friction velocity (u_*). The friction velocity is a velocity scale introduced for convenience from the stress at the surface,

$$u_* = (\tau_0/\rho)^{0.5}. \tag{1.2}$$

As the stress at the surface is only dependent on viscosity, so is u_*. From dimensional analysis,

$$\frac{U}{u_*} = f(z_1), \tag{1.3}$$

where $z_1 = u_*z/\nu$ is the non-dimensional vertical coordinate. In the lower inner-region, there is a shallow sub-region where fluxes are assumed constant and viscosity dominates. This simplifies Equation 1.1 to

$$\nu\frac{dU}{dz} = \tau_0/\rho, \tag{1.4}$$

where τ_0 is the surface stress. Integrating (1.3), we get a region with a linear velocity profile known as the viscous sublayer,

$$U = u_*z_1. \tag{1.5}$$

Away from the surface, called the outer-region, viscosity is not directly important and the Reynolds stress is dominant in τ. The Reynolds stress, throughout the column, is proportional to the viscosity dominated surface stress. This may seem counter-intuitive but is reasonable as the steady-state assumption implies coupling of the whole boundary layer. The parameters of the problem are therefore U, u_*, z, the free-flow velocity (U_∞), and the boundary-layer depth (D). Considering the velocity deficit in the boundary layer, dimensional analysis results in,

$$\frac{U - U_\infty}{u_*} = F(z_2), \tag{1.6}$$

where $z_2 = z/D$ is the outer-region's vertical coordinate. Matching the two regimes from Equation 1.3 and Equation 1.6 in the limit of $z_1 \to \infty$ and $z_2 \to 0$, results in

$$z_1 \frac{df}{dz_1} = z_2 \frac{dF}{dz_2} = constant. \tag{1.7}$$

The constant is taken as $1/k$. Integrating for the matched regime results in the LP,

$$U(z) = \frac{u_*}{k} log(u_* z/\nu) + C. \tag{1.8}$$

It is important to note that for a flow over a smooth surface, it is only viscosity which contributes to u_* and therefore solely couples the boundary layer with the surface. Turbulence adjusts to preserve this steady state coupling.

To consider the analogue of this physical system in the atmosphere, the assumption of a smooth surface must be relaxed to accommodate the presence of rougher surfaces (i.e vegetation, oceanic waves, or sastrugi). The drag caused by a rougher surface plays the dominant role over viscosity. Each individual surface feature contributes to an ensemble of roughness elements. A given surface is then attributed, from this ensemble, the statistical property of surface roughness. The lowest layer of the ABL is called the roughness sublayer, and is the layer where the stress is determined not by the ensemble but by individual constituents. The roughness-sublayer plays an analogous role to the viscous-sublayer in establishing u_*, the representing parameter of surface roughness and controlling parameter for turbulence aloft. The ASL is the layer over the roughness sublayer where fluxes are assumed constant and controlled by u_*. This control can be thought of as the arrangement of eddies in the ASL such that the quasi-steady state is maintained. In cases where a quasi-steady state is not achieved, u_* is no longer the controlling parameter and the associated similarity theory fails. The existence of the ASL as a constant-flux layer is associated with similar conditions as Kolmogorov's similarity hypothesis, where an inertial subrange is established (Högström, 1996).

In the ASL, the flow is fully characterized by two independent variables, friction velocity (u_*) and the height (z), setting up the ideal conditions for a similarity theory approach. Pragmatically, this results in a realistic theoretical program that is naturally applied to observations, as u_* can be measured from a point source of data, and if measured in the ASL, fully determines the system. An auxiliary benefit is the surface itself does not need to be resolved as u_* objectively captures the roughness sublayer's influence on the surface fluxes.

When considering the vertical gradient of wind, dU/dz, only one non-dimensional group can be formed and therefore it is constant,

$$k \frac{z}{u_*} \frac{d\overline{U}}{dz} = 1. \tag{1.9}$$

In this work, the von Karman constant, k, is considered the normalization constant of the non-dimensional gradient. Through historical arguments, primarily through mixing-length theory, k is considered to be a universal constant. Several theories have considered a dependence between k and the Reynolds or Rossby number but experimental evidence does not suggest any dependency (Högström, 1996). Integrating Equation 1.9 results in the logarithmic wind profile (lwp),

$$\overline{U}(z) = \frac{u_*}{k} log(z/z_0). \tag{1.10}$$

The constant z_0 is chosen to be the height where $\overline{U} = 0$ and is dependent on the surface properties. A constant-flux layer and the lwp are closely tied phenomena and considered in this work as equivalent. The lwp does not take density stratification into account, making it valid for a neutrally stratified atmosphere. Extensions into the stable and convective regimes is therefore necessary to understand and parameterize the ASL.

The theory is extended to stable conditions through a similarity theory approach. The convective regime is not discussed further. With the addition of temperature to the physical dimension of the problem, the Buckingham Pi theorem requires an additional two physical parameters to add a second non-dimensional group to the one already determined in Equation 1.9. As u_* characterizes the momentum flux, $\overline{w'T'}$ will characterizes the heat flux, again appealing to the constant-flux assumption in the ASL. The last parameter, g/T_0, represents the Archimedian force where T_0 is the reference temperature. The similarity theory derived from these physical parameters is called Monin-Obukhov Similarity Theory (MOST). The non-dimensional group representing the stability is

$$\zeta = -k\frac{zg}{T_0}\frac{\overline{T'w'}}{u_*^3}, \tag{1.11}$$

and is called the stability parameter. The $-k$ is introduced -for convenience- in many presentations. The Buckingham Pi theorem does not specify the constant.

As of yet, the equations of motion have not been considered as the theory results from dimensional analysis alone. From the turbulent kinetic energy (TKE) budget equation, the balance between the shear production and the buoyant destruction of turbulence can be measured in a turbulent flow by the flux Richardson number,

$$R_f = \frac{(\frac{g}{T_0})\overline{w'T'}}{\overline{u'w'}\frac{d\overline{U}}{dz}}. \tag{1.12}$$

When $R_f > 1$ a turbulent flow will decay and when $R_f < 1$ a turbulent flow will remain turbulent. Assuming the wind profile is approximately logarithmic,

$$\overline{U}(z) = \frac{u_*}{k}log(\frac{z}{z_0}) + \epsilon(z), \tag{1.13}$$

where $\epsilon(z)$ is the correction term, R_f can be approximated as follows,

$$R_f = \frac{(\frac{g}{T_0})\overline{w'T'}}{\overline{u'w'}(\frac{u_*}{zk} + \epsilon'(z))} = \zeta(1 - \frac{zk}{u_*}\epsilon'(z) + O(\epsilon'(z)^2)), \tag{1.14}$$

$$R_f \approx \zeta, \quad \epsilon'(z) \ll 1 \tag{1.15}$$

The stability parameter is the first order approximation of the R_f in the ASL about a lwp. A full determination of R_f would require measurements at every level. By approximating about a lwp, only one level of measurements is required to compute the height dependent stability in the ASL. This reduction from the dynamic equations which consist of an infinite number of parameters to the finite system of MOST is promising and provides a tool for interpreting the applicability of MOST. With increasing stability, the wind profile deviates from the lwp and Equation 1.15 no longer holds. When this occurs, it is not clear how ζ should be interpreted.

The main results of MOST are the relations between the non-dimensional gradients and the stability parameter,

$$\frac{kz}{u_*}\frac{d\overline{U}}{dz} = \phi_M(\zeta). \tag{1.16}$$

Similarly for the temperature profile,

$$\frac{kz}{T_*}\frac{d\overline{T}}{dz} = \phi_H(\zeta), \tag{1.17}$$

where $T_* = -\frac{\overline{w'T'}}{u_*}$ is the analogue to u_*. Both ϕ_H and ϕ_M are determined empirically from observations. A turbulent Prantl number can be defined through the ϕ_M and ϕ_H functions,

$$Pr_t = \frac{\phi_H}{\phi_M}. \tag{1.18}$$

This formulation of Pr_t is based off a K-theory understanding of the relationship between fluxes and local gradients. When $Pr_t < 1$ the momentum flux is more efficient than the heat flux and vice-versa. Contrasting work has shown $Pr_t > 1$ and $Pr_t < 1$ (Grachev et al., 2007). As this is an extension of the similarity theory for neutral conditions, $\phi_M(\zeta)$ should converge to 1 when $\zeta \to 0$. Expanding ϕ_M in a Taylor series about $\zeta = 0$, the first order approximation is,

$$\phi_M(\zeta) = 1 + \beta\zeta. \tag{1.19}$$

Equation 1.19 has been shown to be accurate for $\zeta \leq 1$ where $\beta \approx 5$ (Businger et al., 1971; Dyer, 1974; Högström, 1988). Using the condition that $\epsilon'(z) < 1$ in Equation 1.15 with the empirically derived Equation 1.19, an estimate of validity is $\zeta < 0.2$. This range of validity is is similar to the $\zeta < 0.1$ which defined the surface-scaling regime of Grachev et al. (2005). The observed validity of Equation 1.19 is better than theoretically predicted. In strongly stable conditions, the constant-flux layer is often below the measurement level. Instead of considering a surface scaling, i.e with fluxes measured in the constant-flux layer, Equation 1.19 is derived from observations aloft. Is is also observed to have $\beta \approx 5$. This regime is called the local-scaling regime and can be interpreted as a layer with locally near-constant fluxes, i.e a local organization of the eddies. The existence of the local-scaling regime extends the validity of Equation 1.19 past $\zeta = 0.2$. With further increase in stability, rotation becomes significant and non-local effects play a role in the turbulent structure. Under those conditions, the local scaling fails.

From the above discussion, the ASL is understood through analysis of steady-state conditions, where turbulence throughout the column is coupled to the surface. This coupling allows for a similarity theory approach resulting in the determination of empirical functions ϕ_M and ϕ_H. With increasing stability, the layers become decoupled and the ASL is no longer steady. In addition, stable stratification allows for the propagation of waves and introduces a wealth of phenomena. This complicates the structure of turbulence by introducing non-local dependence (Mahrt et al., 2015). The ASL is therefore not governed by the locally measured variables and no similarity theory is achievable. Irregardless of the validity of similarity theory, the definition of ASL is from now on extended to the lowest 10 m of the atmosphere. This is done for pragmatic reasons as the measurement heights for this study are 2 m and 10 m. Additionally, many models, irregardless of its validity, use MOST for the lowest 10 m.

Chapter 2

Methods

A description of the data set, data handling and processing, and eddy-covariance is presented in this chapter. A big part of the thesis work was the processing and development of the data set in a format that allows for convenient interval selection and eddy-covariance calculations. The data processing was done iteratively with continuous improvements on the formatting. The goal was to make the data set readily available for studies in micro- and boundary layer meteorology. All the processing and eddy-covariance calculations were done from scratch, with exception of processing the slow sensor data. This was done by Irene Suomi from the Finnish Meteorological Institute. The reason for not using already established software, for example TK3 (Mauder, 2011), is the black box nature of those packages. Standardized corrections and quality checks which are valid at mid-latitudes may not work for the Antarctic conditions. To understand the behaviour of different methods, a bottoms up approach is adopted. More advanced methods should be applied once the error in the simplest method is established. In this spirit, the following chapters use simple eddy-covariance methods and the validity and possible improvement of the methods are discussed throughout.

2.1   Observations

The data set used in this work is from the *Antarctic Meteorology and Snow Research: from Process Understanding to Improved Predictions* (ASPIRE) project. A research goal of ASPIRE is to study the role of surface turbulent fluxes on the behaviour of the atmospheric boundary layer, as well as on the large-scale conditions. To this purpose, a 10 m mast was deployed at AWS5 during three separate expeditions to Aboa station, Dronning Maud Land (see Section 3.1). The expeditions were coordinated through the Finnish Antarctic Program (FINNARP). The three expeditions occurred during the 2010-2011, 2014-2015, and 2018-2019 seasons, referred to as F10, F14, and F18, respectively. Aboa station is only habitable during the austral summer with operations occurring between December and February. High resolution, eddy-covariance data was collected through two Campbell CSAT3 3D sonic anemometers, installed at 2 m and 10 m. Slow sensors included 2D Gill WindSonic anemometers installed at 6 levels. Campbell 107-type temperature probes were also installed, but due to daytime radiative warming, the temperature derived from the Gill WindSonic will be used instead in the following work. Radiation was measured by a Kipp & Zonen CNR4 radiation budget probe which measure both shortwave and longwave fluxes. The previously mentioned instruments are used in this study, though further observations were collected by

tethersonde and radiosonde launches, 3D SODARs, RPAS flights and a multitude of snow measurements.

In addition to data collected at Aboa station, the geopotential height for the 850 HPa level was extracted from ECMWFs ERA-Interim reanalysis.

2.2   Data Quality and Processing

The data processing is described in this section for the CSAT3 sonic anemometer. Similar processing was performed for the slow sensors. Figure 2.1 is a schematic of the data process-ing, where *A* through *D* represent the steps taken. The *REPOSITORY* block is the directory with all of the output of the logging systems deployed during the expeditions. This will in-clude the full data of every system. For example, the directory of the 10 m CSAT3 data is *~/2010-Antarc/00DATA/AWS5/Flux/10m/*.dat* . For the CSAT3, the logger saved daily files. In cases where the system was turned off and on, file repetition occurred and lines were often broken. Step *A* removes all broken lines and merges repetitions into single daily files, i.e the *.dat files* block in Figure 2.1. This block allows for easy looping over the full data set. The data at this points includes $time$, represented in a numeric format of *YYMMDDhhmmss*, X, Y, Z velocities in m/s, the sonic temperature T_s in $°C$, and the quality flags. Step *B* starts treating the data through one hour segments, this was deemed the easiest partitioning of the data set. Looping over each hour interval, if the *NaN* count is greater that 0.1% of the data, the hour interval is discarded. This may seem harsh but without knowing the source of error these intervals are not reliable. The time series are then interpolated to 20 Hz. This step is necessary as 20 samples per second is not always achieved depending on the logger routine. The 20 Hz data is then saved to a *NetCDF* group *RAW* in hourly *NetCDF* files. The hourly files are named -*YYMMDDhh.nc*-. The *RAW* group consists of the variables $time$, X, Y, Z, Ts, *time_old*, *flag_old*, and *flag_int*. The variables *time_old* and *flag_old* are the times printed by the logger as well as the built in flags. Additionally, *flag_int* shows the occurrence of *NaN* values for the initial time series, with *flag_int* = 3 when values are *NaN*, otherwise *flag_int* = 0. The collection of *RAW NetCDF* groups is referred to as the block *RAW* in Figure 2.1.
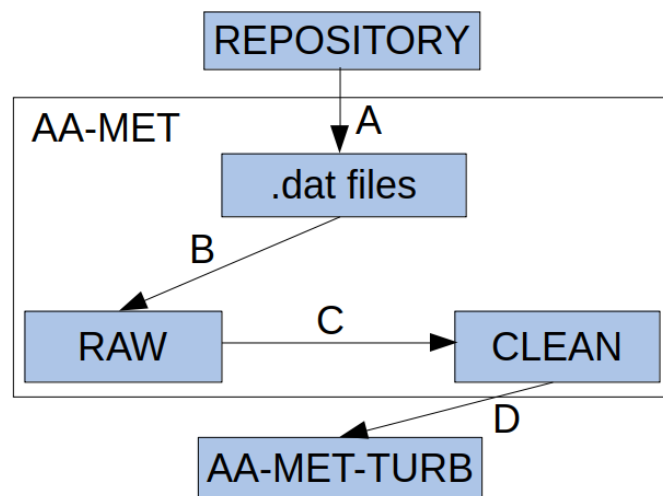

Figure 2.1

Step C is the step where the data is cleaned. This includes spike removal and the removal of unphysical data. The $time$ variable is also reformated during step C to *numpy*'s *datetime64[ms]* format. Time intervals with missing values are now padded with NaNs to ensure an evenly spaced time array, simplifying and accelerating subsequent routines considerably. For spike detection, a novel method was applied which extends the methods of Suomi et al. (2017) and Hejstrup (1993). For a time series $\{u_i\}$, a forecasting method is used to predict each point, i.e $\{u_i^{fcst}\}$. A point u_j is considered a spike when it deviates significantly from u_j^{fcst}. The forecast used for u_j is,

$$u_j^{fcst} = \rho_\Delta u_{j-1} + (1 - \rho_\Delta)\overline{u}^\Delta, \tag{2.1}$$

where ρ_j^Δ is the correlation coefficient of subsequent points,

$$\rho_j^\Delta = \frac{cov(u_n, u_{n+1})}{\sigma_\Delta^2}, \tag{2.2}$$

and Δ is the calculation window about u_j and is not specified at this point. The forecast equation is interpreted as a weighted average of the previous value and the local mean, where the weight is the correlation coefficient. The point u_j is a spike if

$$|\frac{u_j^{fcst} - u_j}{\sigma_\Delta}| > C_{spike}, \tag{2.3}$$

holds for a selected C_{spike} value. As of yet, the method is the same as applied in Suomi et al. (2017). The novel extension comes from the fact that a spike should be independent of the position of Δ about u_j. Given two different windows, for u_j to be considered a spike, it should be a spike for both windows. The spike detection used implements the two extreme choices for Δ, i.e when u_j is the leftmost and rightmost point in Δ. Additionally, the spike detection method is used iteratively. Once the spikes have been found and replaced through linear interpolation, the spike detection method is applied again with $C_{spike} = C_{spike} + 0.1$, until no more spikes are found. The initial value of C_{spike} was 4 and 4.5 for velocity and temperature, respectively. The window size, $|\Delta|$, was chosen as 80 points or 4 seconds. The spike detection is not sensitive to the above choices.

Values which are considered unphysical are removed through linear interpolation. The following ranges are deemed physical, $-25°C < T_s < 20°C$, and X, Y, $Z < 35$ m/s. These values were chosen from what is realistic and expected around the area of study.

The time series of X, Y, Z, and T_s, after the spike removal and filtering of unphysical values, is added to the hourly *NetCDF* files. This group is called *CLEAN* as seen in Figure 2.1. This group also includes the variable $flag$. For points where there were spikes, unphysical values, and NaNs, $flag = 1$, 2, and 3 respectively.

The *.dat files*, *RAW*, and *CLEAN* blocks constitute what is called the *AA-MET* data set after Aboa AWS5 METeorology. The data of *AA-MET* only has a quality criteria for the number of NaN values observed. Before the data is ready for eddy-covariance calculations, additional quality criteria must be met in step D resulting in the *AA-MET-TURB* data set.

For an hour segment to qualify for *AA-MET-TURB*, the following conditions must be met:

1. Every second must be sampled at least 10 times.

2. The maximum NaNs-per-minute must be lower than 0.1%

3. The maximum spikes-per-minute is less than 1%

4. Every one minute interval in the hour must have

    (a) $-25 < \overline{T_s} < 20$
    (b) $10^{-6} < \sigma_{X,Y,Z,T_s} < 10$
    (c) $\overline{X}, \overline{Y}, \overline{Z} < 35$

5. For periods with wind speed greater than 3 m/s, the 10 minute mean wind directions should not be from the shadow of the mast ($260°$ - $280°$).

Only the *AA-MET-TURB* data set is used in this work and is discussed further.

2.3 Eddy-Covariance

The eddy-covariance methodology in this work is kept as simple as possible. Many issues in eddy-covariance are unresolved and vary between different studies. For a discussion on eddy-covariance in the Arctic, see Sjöblom (2014). In this work four aspects are important to address: the role of moisture, choice of averaging window, the alignment of the CSAT3, and the computation of the vertical gradients of temperature and wind speed. Eddy-covariance should always be done iteratively, continuously improving on the methods as they are dependent on the properties of the data set in question.

2.3.1 Humidity correction

The CSAT3 sonic anemometers measure sonic temperature (T_s) from the speed of sound. It has been noted that T_s is almost equivalent to virtual temperature (Sjöblom, 2003). From virtual temperature, the humidity correction of Schotanus et al. (1983) can be applied. At AWS5, the near-surface humidity is around 0.5-3 gkg^{-1} resulting in a temperature correction of $0.3°C$ (Nygård et al., 2017). Humidity is therefore negligible for the conditions around AWS5. For the following, temperature always refers to the sonic temperature.

2.3.2 Averaging window

The choice of the averaging window, for flux calculations, is a sensitive subject for stable boundary layers. The ubiquitous presence of mesoscale phenomena with scales approaching the scale of turbulent eddies, confuses the definition of the mean and perturbations off the mean (Mahrt, 2014). A strict definition of turbulent kinetic energy (TKE) is only valid when the mean flow is well defined. A rigorous method of determining averaging length is by considering the cospectra of temperature and vertical velocity, known as an ogive (Kilpeläinen and Sjöblom, 2010). Ogive analysis is beyond-the-scope of this work where the choice of a window length is made between 30 minutes and 10 minutes. Longer windows of 1 hour are used, but due to the unstationary nature of the signal, it is far too long for the observed conditions. To determine the difference in flux calculations between a window size of 10 minutes and 30 minutes, the relative difference function,

$$\delta_X = \frac{X_{30} - X_{10}}{\mid X_{30} \mid},$$

(2.4)

was computed for TKE, kinematic heat flux ($\overline{w'T'}$), and friction velocity (u_*) .
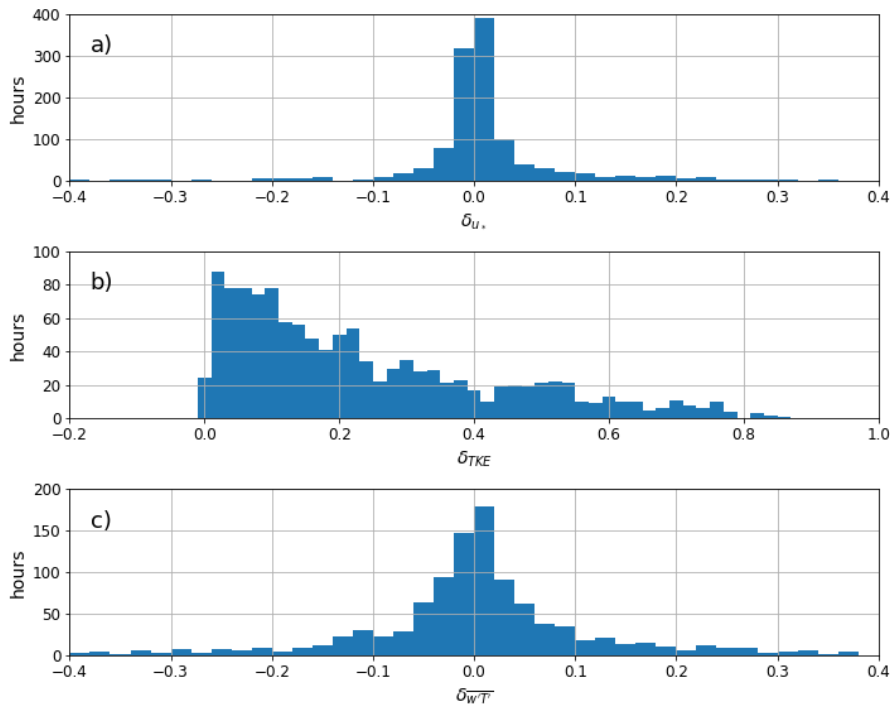

Figure 2.2: The relative difference between the 30 minute and the 10 minute fluxes for a) friction velocity, b) turbulent kinetic energy, and c) kinematic heat flux.

From Figure 2.2, it was found that for the friction velocity, TKE, and $\overline{w'T'}$, the $\pm 10\%$ relative difference range contained 88%, 35%, and 73% of the data, respectively. The difference between u_* and TKE can be interpreted as the TKE is capturing variance in the mean variables which are not cross correlated. The lack of convergence between the 30 minute and 10 minute fluxes implies that a 30 minute window is too long for this data set. All fluxes in the following work are computed for a 10 minute averaging window.

2.3.3   Tilt correction

A large source of error in vertical flux calculations is the misalignment of the CSAT3 in relation to the flow. This error comes from misalignment of the instrument in relation to the ground and flows which are not purely horizontal. Due to the horizontally homogeneous conditions near AWS5, the later is not considered further. Three methods are used to align the Cartesian coordinates of the instrument with the flow; the double-rotation, triple-rotation and planar-fit methods (Wilczak et al., 2001; Kral et al., 2014). The double-rotation method first rotates the xy-plane into the mean wind direction and then a second rotation projects the mean vertical velocity onto that direction. This ensures that if x is the mean wind direction, $\overline{v} = 0$ and $\overline{w} = 0$. This method is not perfect. If we suppose the CSAT3 is tilted only in the x-direction then the vertical velocity will have erroneous contributions from the flow from that direction. This will rotate the mean wind vector counter-clockwise and the mean vertical velocity will be projected onto the wrong direction. Errors in the resulting stresses are discussed in Wilczak et al. (2001). The triple rotation adds an additional rotation to ensure that the cross-mean stress is zero, $\overline{v'w'} = 0$. This is not desirable for stable conditions where

mesoscale motions can force cross-mean stresses. The most accurate method is the planar-fit method which minimizes the mean vertical velocity through multiple linear regressions. The disadvantage is that planar-fit requires a large data set and cannot be applied in real time. Comparison of the double-rotation and planar-fit methods, for Arctic conditions, is presented in Kral et al. (2014). For the sake of simplicity, the double-rotation was chosen for the following work.

To understand the initial tilt error, Figure 2.3 plots the tilt error in terms of wind direction. If $[x, y, z]$ are the initial coordinates with associated velocities $[X, Y, Z]$, the tilt error is defined as,

$$E_T = \frac{|\overline{Z}|}{(\overline{Y}^2 + \overline{X}^2)^{0.5}}. \tag{2.5}$$

Figure 2.3 plots $[E_T, arctan(Y/X)]$. The observed pinching off of error is the direction perpendicular to the plane of misalignment. Out of the three campaigns, F18 was most prone to tilt errors.
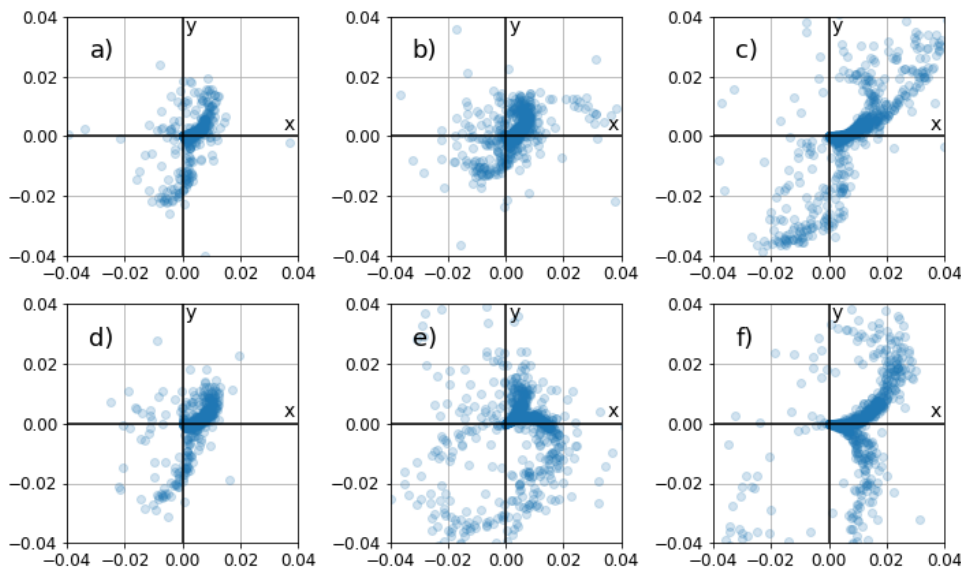

Figure 2.3: Tilt error in polar coordinates. Panels a), b), and c) are for the 2 m CSAT3 for the F10, F14, and F18 campaigns. Panels d), e), and f) are equivalent for the 10 m CSAT3.

2.3.4   Gradient calculation

The computing of vertical gradients for the mean wind speed and temperature is strictly speaking not a part of eddy-covariance, but its role in MOST is critical. Different interpolation schemes can be used, including linear, logarithmic and second-order polynomial fits (Grachev et al., 2007; Forrer and Rotach, 1997). There is no -best method-, as the performance of a certain method is dependent on the curvature of the profiles. Once again, for simplicity the linear fit is used in this work and its validity addressed when necessary. For the F10, F14, and F18 expeditions, the slow sensors used for the gradient calculations were are 1.2 m and 5 m, 1 m and 6 m, and 1 m and 4 m instruments, respectively.

Chapter 3

General Conditions over DML

When investigating the structure of turbulence and other dynamic phenomena in the ASL, the greatest weakness is the pointwise nature of high resolution observations. This under-sampling of the complicated three-dimensional flow in the atmosphere can easily result in misinterpretation of the observations. The simplest example is the arrival of a sloped front of some scalar variable. What is in fact a change in the measurements due to an advective process can be misinterpreted as an expansion or contraction. Sampling the atmosphere using multiple platforms simultaneously is a solution to this problem and improvements on standard observational strategies are being implemented (Kral et al., 2018).

To respect the three-dimensional nature of the flow, any analysis on turbulence and small-scale features of the ASL should be preceded with analysis of the mean conditions and the development of a general understanding of the area. This is the main purpose of this chapter. Section 3.1 addresses the geography of the area. Section 3.2 presents the general statistics of the mean meteorological variables as well as full campaign time-series. The observations at AWS5 from *AA-MET-TURB* are compared to previous campaigns at AWS5, as well as other locations in DML. Lastly, Section 3.3 addresses the diurnal cycle at AWS5.

3.1   Geography and History

The AWS5 site described in Section 2.1 is located 10 km to the south-east of Finland's Aboa Station in western DML (Figure 3.1). AWS5 is located at [13.17°W, 73.11°S] on a snow covered glacier 296 m above sea level. The local slope has a declination angle of 0.6° to the north. AWS5 is 130 km south-east of the open Weddell Sea, passing through the Riiser-Larsen ice shelf. The area of AWS5 is classified as part of the coastal katabatic zone (Van den Broeke et al., 2005). In addition to Aboa station, coastal DML is host to Germany's Neumayer Station III, 350 km to the north-east on the Ekstrom ice shelf, and England's Halley Station, 455 km to the south-west on the Brunt ice shelf. There are several other Antarctic stations in coastal DML, but they are not considered in this work.

The wind direction at AWS5 is predominantly from the east where the flow is almost undisturbed for over 100 km. Around 200 km to the south of AWS5 is the Heimefrontfjella and Kirwanveggen mountains, separating the region of study from the Antarctic plateau. The Heimefrontfjella is host to Svea, a Swedish Antarctic station. Further south on the plateau is Germany's Kohnen Station. The Antarctic plateau is followed by a steep drop of 500 m before gently sloping down to the Vestfjella mountains. The inland sloped regions are clas-

sified as the inland katabatic zone (Van den Broeke et al., 2005). Aboa station is located on
the Basen nunatak, a member of the Vestfjella mountains with its peak at 350 m above the
underlying glacier. The Basen nunatak is the predominant feature of the area around AWS5,
though AWS5's location was chosen to minimize the influence of the nunatak. A possible
local effect on the observations at AWS5 are upstream propagating gravity waves generated
over the Basen nunatak. This was determined not to be the case by Valkonen et al. (2010),
who determined through WRF simulations that gravity waves exist in a regime where they
remain over or downstream of the nunatak. Additionally, there are blue ice area's in the vicin-
ity of the Basen nunatak, but the range of influence of the blue ice does not reach AWS5.
AWS5 as seen by its name was originally the location of the 5th automatic weather station
(AWS) in a network of dutch stations deployed around DML. AWS1 to AWS3 were de-
ployed in January 1997, spread around the Prime Meridian (van den Broeke et al., 1999),
and AWS4 to AWS8 were deployed the following year in a transect around 12°W (Holm-
lund et al., 2000). An additional station, AWS9, was installed on the Antarctic plateau. The
AWS network resulted in around two years of data, referred to as *dutch-AWS* in the follow-
ing. The results published through *dutch-AWS* allows for comparison with *AA-MET-TURB*
and for the consideration of the interannual, seasonal, and spatial variability of the mean me-
teorological conditions. Four of the AWS are of particular importance, AWS4 represents the
coastal ice shelf, AWS5 the coastal katabatic zone, AWS6 the interior katabatic zone, and
AWS9 represents the Antarctic plateau.

The location of AWS5 is ideal for fundamental studies in boundary layer meteorology, as
there are little to no local effects due to horizontal inhomogeneity, and supporting data sets
(*dutch-AWS*) allow for the generalizing and contextualizing of the results.
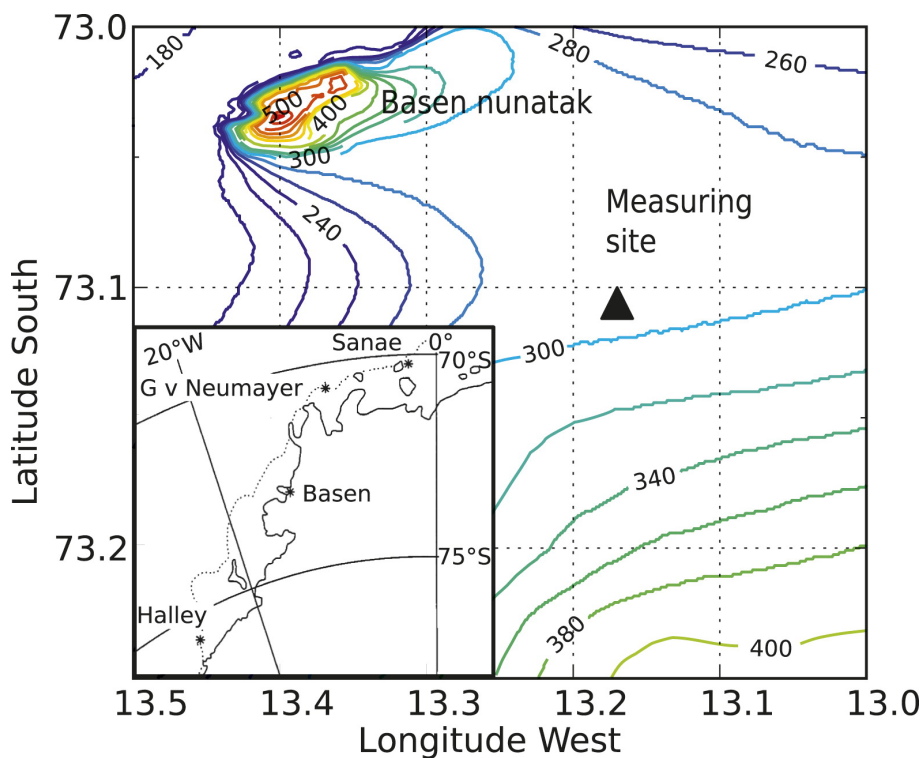

*Figure 3.1: Geographical position of the AWS5 measurement site taken with permission from
Kouznetsov et al. (2012). The main panel shows the orientation of AWS5 about the Basen nunatak
while the sub-panel shows the position of Basen to the rest of western DML.*

3.2   Mean Conditions

The hourly means of wind speed, wind direction, temperature, geopotential height, and radiation, for the full F10, F14, and F18 data sets, are presented in Figures 3.2, 3.3, and 3.4. Throughout this chapter, the F14 campaign exhibits different behaviour from F10 and F18. Noticeable differences are seen visually from the time-series. During F10 and F18, the temperature reaches $0°$, while for F14 the temperature remains colder than $-1°C$.
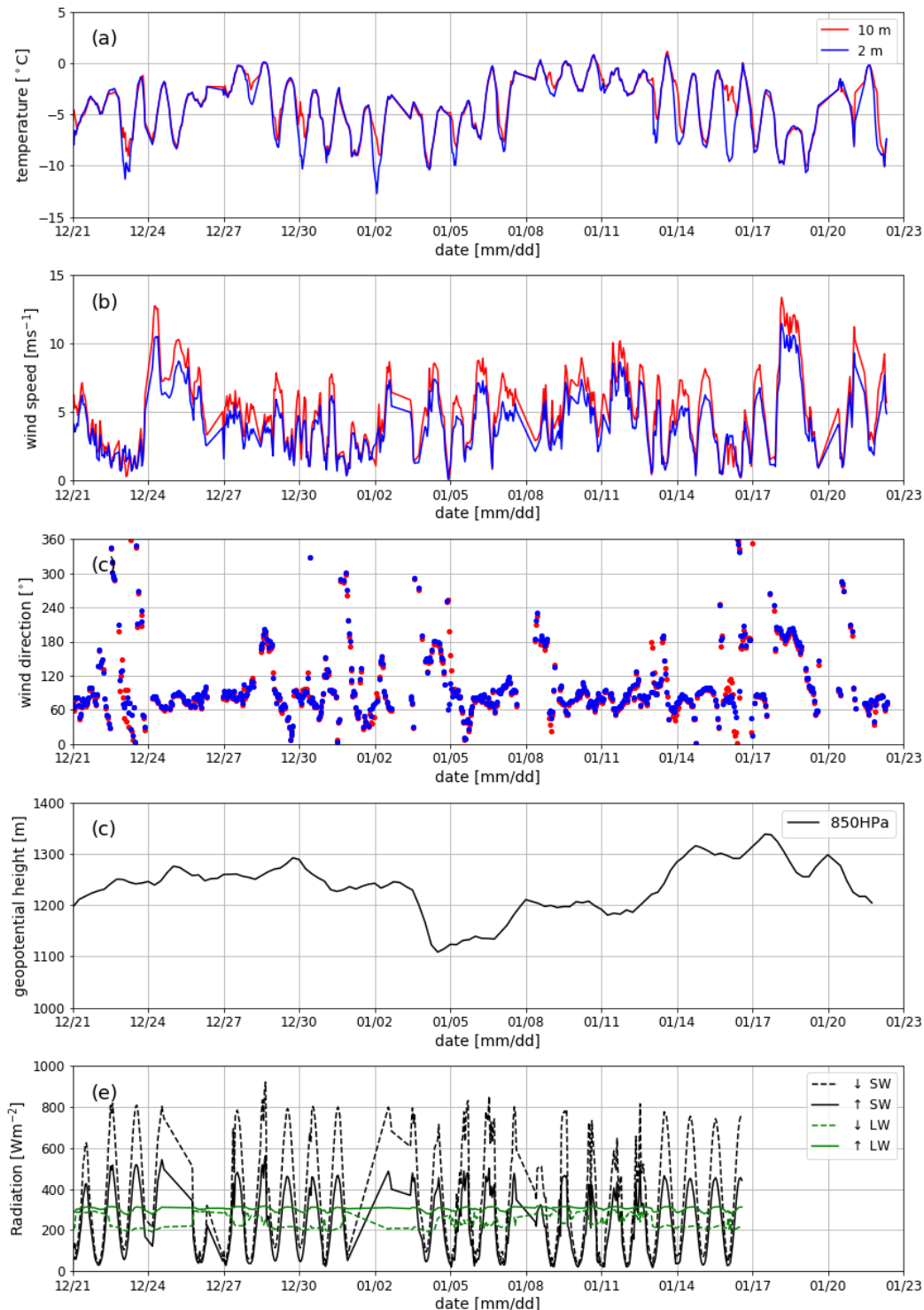

Figure 3.2: Hourly time series of the F10 campaign.

The diurnal cycles is less pronounced for F14. Additionally, the wind speed during F14 is less consistent than for F10 and F18, with a period of weaker winds in December followed by stronger winds in January. During the observational period of *AA-MET-TURB*, two interesting features are worth noting. Firstly, storms were stronger during the F18 season than the previous two. Two major storms occurred during F18. The first starting the 17th of December, lasting two days, and the second the 18th of January, lasting for three days.
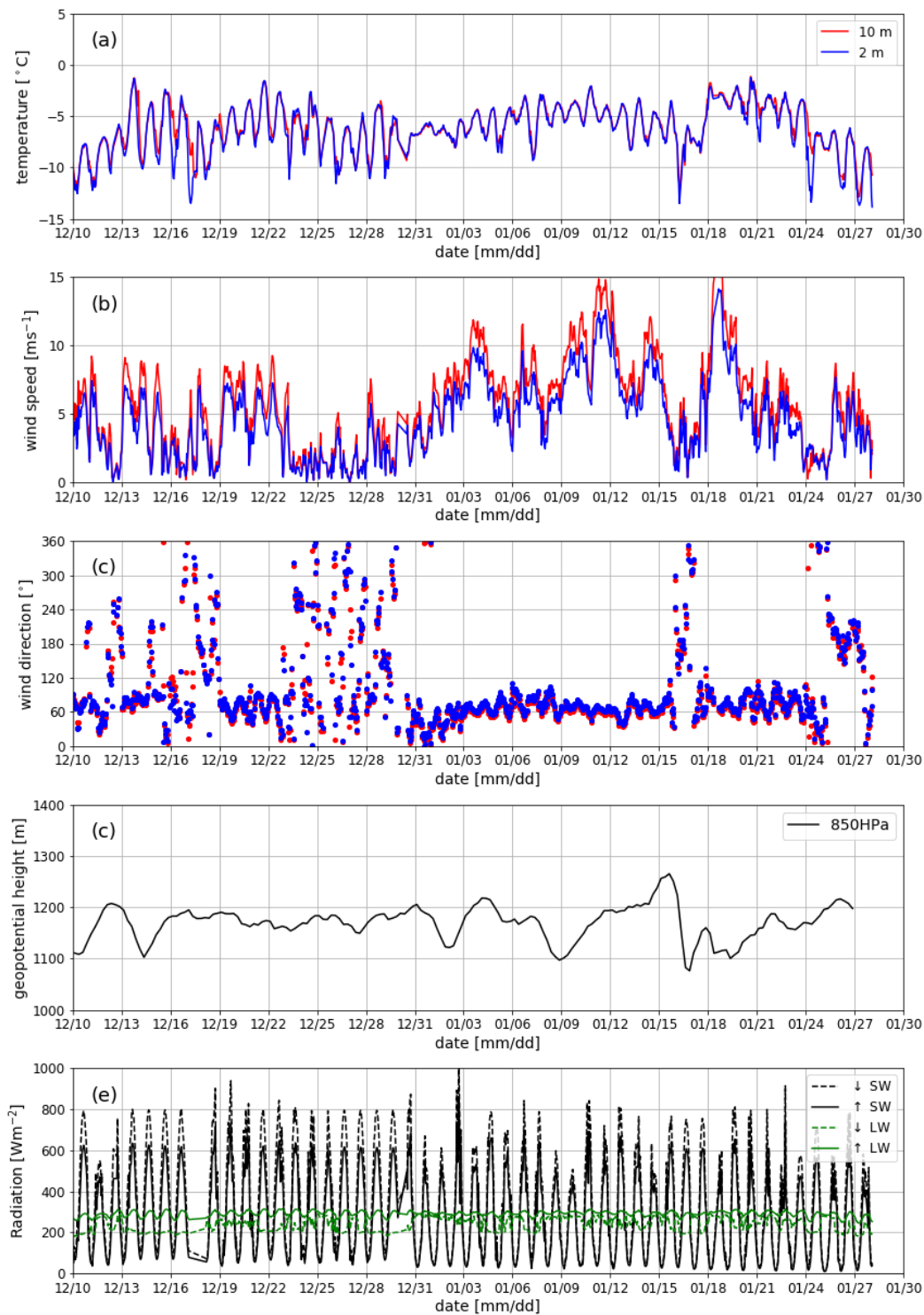

Figure 3.3: Hourly time series of the F14 campaign.

Unfortunately, the instruments did not withstand the strain, and no data was collected during the two major storms. From the time-series, it is reasonable to guess that the maximum hourly-mean wind speed reached 20 m/s. For the second storm, there is an impressive decrease in geopotential height, where the 850 HPa almost reached 1000 m. The second interesting feature is that the F14 campaign had almost a week long period with very weak winds, between the 23rd and 29th of December. During this week, the geopotential height showed little to no variations.
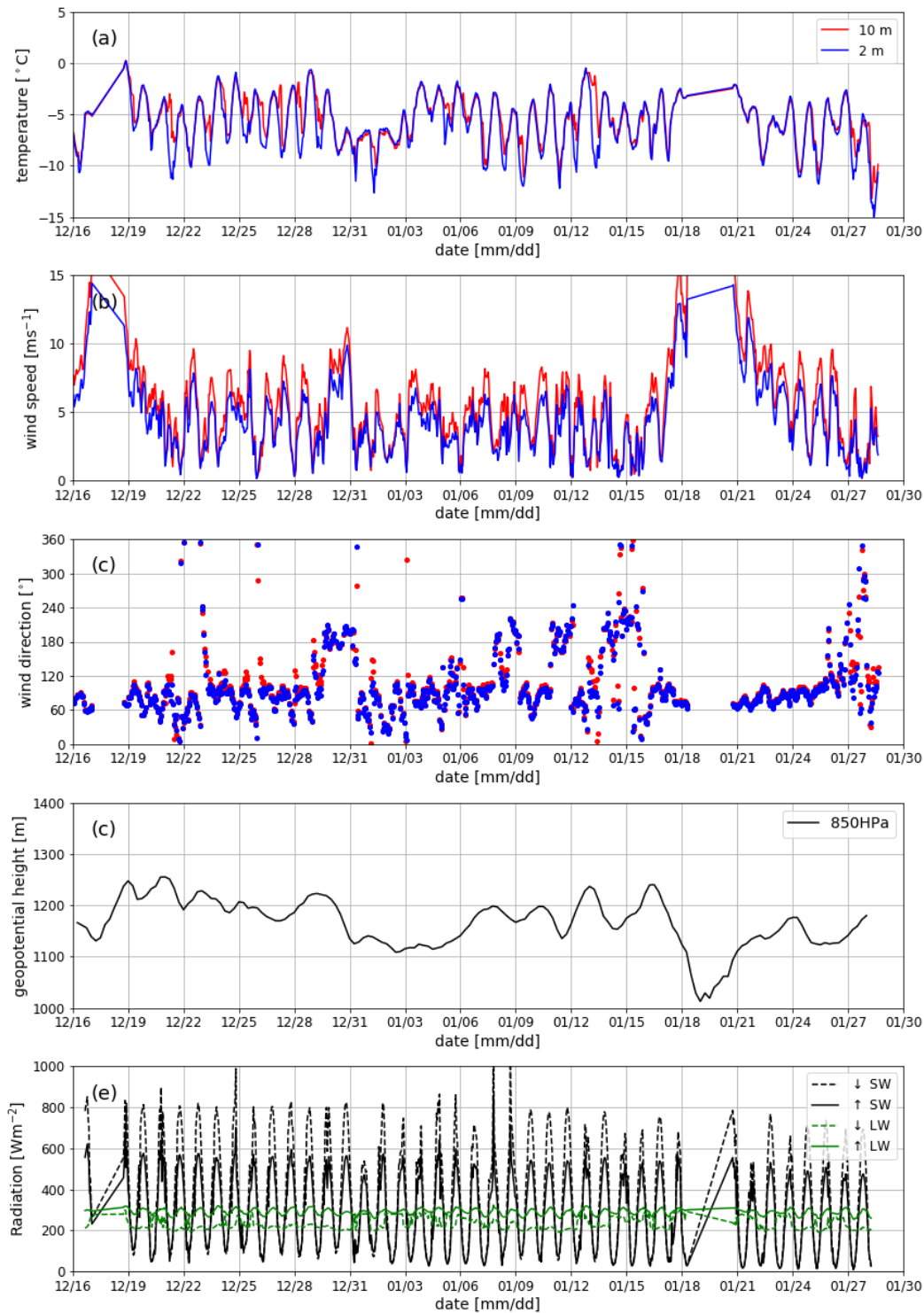

Figure 3.4: Hourly time series of the F18 campaign.

The mean wind speed, wind direction and temperature for the 2 m and 10 m heights are presented in Table 3.1. It should be noted that the mean wind speed is always referring to vector averaging and not the scalar mean. Values in this section are computed using the CSAT3 data because of its significance in the next chapters. This is accurate for temperature and wind speed, though introduces error in wind direction due to the tilt error of the instrument (see Section 2.3). The tilt error is most pronounced in the F18 data for the 10 m instrument.

Table 3.1: Mean summertime conditions at AWS5 for the AA-MET-TURB data set.

AA-MET-TURB						
	F10		F14		F18	
Height [m]	2	10	2	10	2	10
wind speed [ms^{-1}]	4.2	5.1	4.7	5.7	4.5	5.5
Temperature [°C]	-4.5	-4.0	-6.3	-6.1	-5.9	-5.4
wind direction [°]	85	84	76	72	89	95

The mean for *AA-MET-TURB* shows that the temperature at 2 m is around 0.5° colder, and the wind speed about 1 m/s slower than at 10 m. Interannual variability is of the order of 2°C for the mean temperature and 1 m/s for the mean wind speed. The F14 data shows a different character than F10 and F18 with stronger winds, lower temperatures, and the wind from a more northerly direction. From the *dutch-AWS* data set, Van den Broeke et al. (2006) reported a mean 2 m summertime temperature of -9°C, and 10 m wind speed of 7 m/s. Their summertime average was computed between Julian days 296 to 51, a longer period than the *AA-MET-TURB* data set. The increased interval results in lower mean temperature and higher mean wind speed, as expected from the change to Antarctic winter conditions. The *dutch-AWS* data is in agreement with *AA-MET-TURB* that the interannual variability of temperature is about a degree. *AA-MET-TURB* shows larger variability as the seasons are separated by multiple years.

Temperature and specific humidity's annual cycle is highly correlated and regular for all AWS, while the annual cycle for wind speed is more pronounced for the coastal and interior katabatic zones (Reijmer and Oerlemans, 2002). Wind speed maximums are observed in May and August, reaching a monthly mean of 9 m/s. Temperature differences between AWS4 and AWS6 are not significant with a minimum monthly mean temperature between -25°C and -30°C. In contrast, the monthly mean temperature at AWS9 reaches -60°C in April and May. When comparing AWS5 with coastal AWS4, and inland AWS9, Reijmer and Oerlemans (2002) found that during the summer months, the temperature decreased with distance away from the coast. This is expected as inland stations are at a higher altitude. The December and January monthly mean temperatures at AWS4 ranged from -4°C to -6°C, and at AWS6, from -10°C to -12°C. The summertime temperature trend is reversed in the winter, where the warmest temperatures are found to occur over the slopes. This is a result of the wind speed's annual cycle associated with katabatic forcing. Strong low level flows mix warm-air aloft down establishing a potential temperature inversion.

The geographical position of the observation sites plays an equally important role on the wind speed as the local slope. Halley station, though further south, has an annual mean wind speed of 6.2 m/s while for Neumayer it is 8.9 m/s (König-Langlo et al., 1998). AWS5 is closer to the Halley regime with an annual mean wind speed of 6.4 m/s (Reijmer and Oerlemans, 2002).

There are two possible explanations for this difference, Neumayer is located in a stronger katabatic confluence zone and/or positioned closer to the centres of the low-pressure systems over the polar ocean. It is the latter.
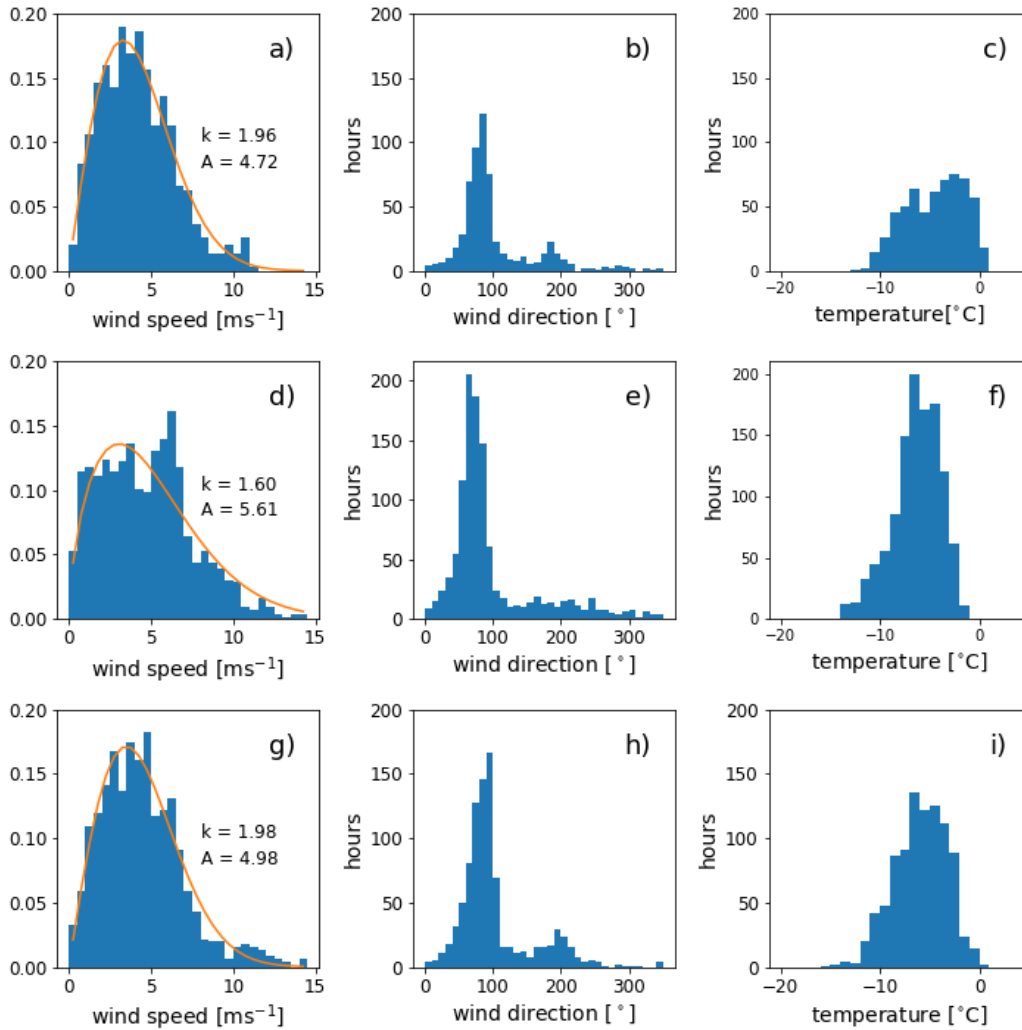

Figure 3.5: The distributions of the 1h wind speed, wind direction, and temperature for the F10 (a, b, c), F14 (d, e, f), and F18 (g, h, i) data sets at 2 m. The wind speed histograms were normalized to make comparisons with the Weibull distribution (orange lines).

Figure 3.5 shows the normalized distribution of wind speed, as well as histograms of wind direction and temperature for each campaign. The wind speed distributions in Figure 3.5 shows that the wind speed distributions peaks at 4 m/s and the maximum hourly mean is 14 m/s. It should be noted that hourly means observed at Aboa station have reached 35 m/s, implying the stronger winds near the station are due to orography (Kärkäs, 2004). To compare the observed wind speed distributions with the wind climatology of other regions in the world, the distributions are fitted to the Weibull distribution,

$$f(x) = k\frac{x^{k-1}}{A^k}e^{-(\frac{x}{A})^k}, \tag{3.1}$$

where A is the scale parameter and k the shape parameter (Weibull, 1951). Another possible distribution for wind speed is the Rayleigh distribution, which is equivalent to Weibull when

k is fixed at 2. For many observation especially in northern Europe, the wind speed follows the Rayleigh distribution (Troen and Lundtang Petersen, 2012). This is also the case for the F10 and F18 data which had $k \approx 2$, but not for F14 which has a k value of 1.6. Figure 3.5 shows that the lower k value of F14 is caused by the Weibull distribution not capturing the bimodal peak structure. This bimodal structure is due to the changes between the low winds of December and the high winds of January observed during F14. The scale parameter, A, is related to the mean wind speed by,

$$\overline{U} = A\Gamma(1 + \frac{1}{k}), \tag{3.2}$$

where $\overline{U}$ is the mean wind, and Γ is the gamma function which for $k = 2$ is around 0.9. The scale, A, was computed at 4.7 m/s, 5.6 m/s, and 5.0 m/s for F10, F14, and F18 respectively, which is consistent with our computed values of Table 3.1.

Figure 3.5 shows two dominant modes of the wind direction, a primary mode around 80° and a secondary mode around 180°. As mentioned, the wind direction is prone to alignment errors though the general pattern is accurate. To quantify these modes for F10, F14, and F18; 69%, 66%, and 70% of cases lie in 50° to 110°, while 11%, 7%, and 12% of cases lie in 170° to 230°. As with the wind speed, the F14 data shows some irregular behaviour in comparison to F10 and F18, with smaller relative occurrences in both the 50° to 110°, and the 170° to 230° sectors.

A wind bimodal structure is a common feature in coastal Antarctica and reflects the two leading forcing mechanisms of antarctic wind, synoptic pressure gradients and the katabatic force (König-Langlo et al., 1998). A useful technique, used in König-Langlo et al. (1998) to illustrate these modes, is plotting a 2D frequency distributions of wind speed and wind direction. Neumayer has two leading modes at [85°, 12 m/s] and [185°, 5 m/s], representing the synoptic and katabatic modes respectively. Similarly, Halley's modes are [95°, 5 m/s] and [185°, 5 m/s]. The stronger annual winds at Neumayer is partly due to the stronger synoptically driven easterly flow, in comparison to Halley's weaker katabatic wind. A second feature at Neumayer is a broader distribution of wind speed for each wind direction, contributing to the mean. The important feature to realize for the modes of Halley and Neumayer, is that they switch locations. The easterly flow at Halley is katabatic while at Neumayer it is synoptic, the south-westerly flow at Halley is synoptic while at Neumayer it is katabatic.

To consider the situation at AWS5, the 2D frequency distributions of the summertime wind speed and wind direction are plotted in Figure 3.6. As F10 and F18 are similar, only F10 was plotted in panel a) and as F14 is different in character, it is plotted in panel b). The leading summertime modes for F10 and F18 are [80°, 4 m/s] and [180°, 4 m/s], the second mode is a lot weaker than the secondary modes at Neumayer and Halley. This can be explained as AWS5 is in a similar katabatic zone as Halley and a similar synoptic zone as Neumayer, resulting in the strong leading mode at 80°. The weak secondary mode at AWS5 is a second synoptic mode related to pressure systems active around Halley. During F14, no such second synoptic mode is present but two modes are present around 80° with wind speed of 4 m/s and 6 m/s. Again, the bimodal structure is due to the contrasting conditions of December and January.
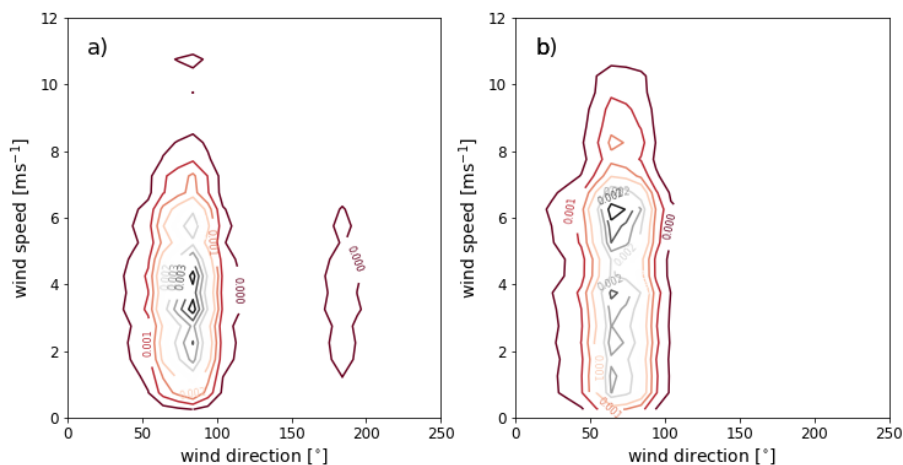
Figure 3.6: The 2D Relative frequency distribution for wind speed and wind direction. For a) F10 and b) F14.

3.3 Diurnal Cycle

The *AA-MET-TURB* data set is entirely during the polar day. Irregardless, the ASL exhibits a diurnal cycle similar to the diurnal cycle of the mid-latitudes. This is due to the variations in the solar zenith angle. Figure 3.7 shows the mean radiation per time-of-day. Downward shortwave radiation has a maximum at 13:00, with an amplitude of around 780 Wm^{-2}, it then approaches zero during the evening hours. The surface energy balance becomes negative at 20:00 and positive again at 5:00, with the minimum occurring between 0:00 and 2:00. This is consistent with the observations of katabatic flows discussed in Section 4.2. The three campaigns have significant variations in albedo with the largest albedo occurring for F14, followed by F18 and F10. Variations in albedo between seasons are most likely due to variations in the sastrugi and snow cover. The albedo has a diurnal cycle due to the solar zenith angle. Additionally, the diurnal cycle of snow grain properties can further attenuate the albedo (Pirazzini, 2004). The mean temperature, wind speed, and wind direction per time-of-day is presented in Figure 3.8. The temperature exhibits a diurnal cycle with an amplitude of around 7 $°C$, 4 $°C$, and 6 $°C$ for F10, F14, and F18, respectively. Annual variations are significant with the F14 campaign exhibiting a mean diurnal cycle with a 3 $°C$ weaker amplitude than F18's. The minimum temperature occurs at around 4:00 for each campaign, and therefore has a delay from the minimum of the radiative cooling. The maximum temperature occurs at 16:00. A diurnal cycle is clear for wind speed, with an amplitude of 2 m/s and a maximum at 6:00 for F10, F14, and F18. The minimum wind speed is not constant for the campaigns, occurring at 18:00, 20:00, and 18:00 for F10, F14, and F18, respectively. Once again, F14 has a different character than F10 and F18. The maximum wind speed occurs after the transition to a positive surface energy balance. Explaining this feature through katabatic forcing is therefore not direct. The diurnal cycle of wind speed is less pronounced in the F14 campaign. Due to the presence of katabatic forcing, if there is misalignment between the directions of the katabatic and synoptic forcing, a diurnal cycle should exist for wind direction. This is weakly existent in Figure 3.8. The wind in the early morning comes from a slightly more southerly direction.

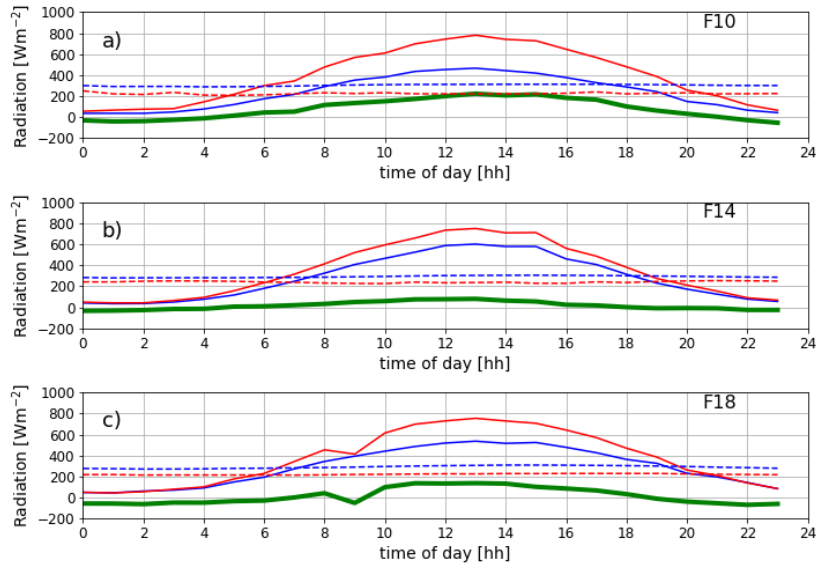*Figure 3.7: Diurnal cycle of radiation for a) F10, b) F14, c) F18. The dashed lines are longwave radiative, solid lines shortwave radiation. Blue is outgoing, red is incoming. The green line is the net radiation.*
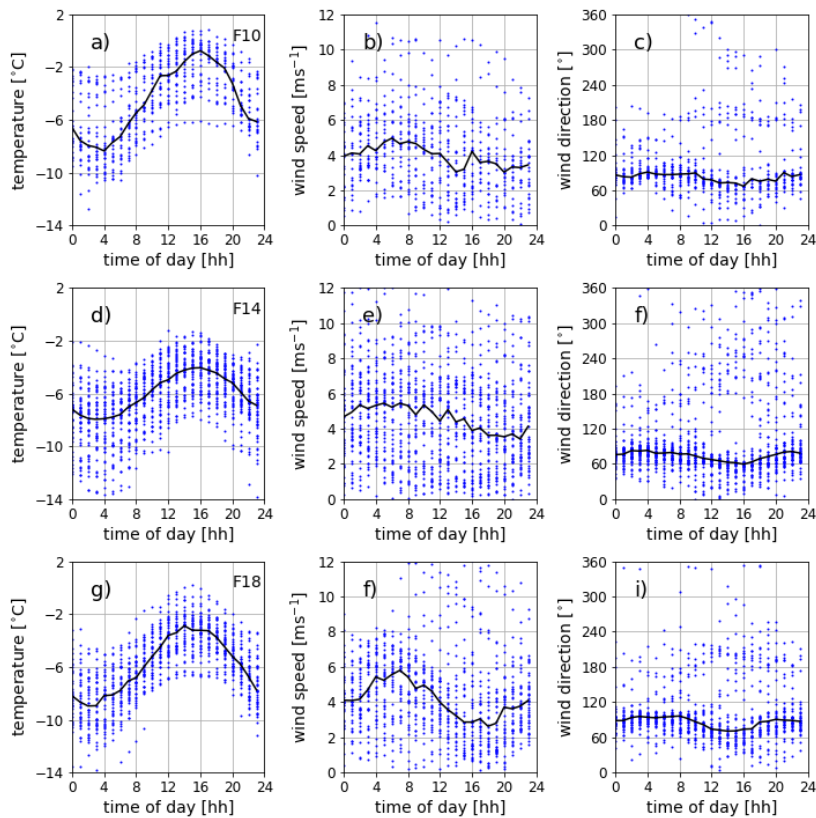

Figure 3.8: Diurnal cycle of temperature, wind speed, and wind direction. a)-c) is for F10, d)-e) for F14, g)-i) for F18. The full data is in blue, the median is plotted in black.

Chapter 4

The phenomenology of the ASL over DML

This chapter provides an overview of some of the different ASL phenomena observed at AWS5. Phenomena superposed on a mean flow introduces an oscillatory component to the observed signal. For that reason, the Eularian autocorrelation function (EAF) is chosen as the main tool for this chapter. Additionally, EAFs are commonly used in the study of wind meandering (Anfossi et al., 2005).

The understanding of different ASL phenomena, and their role in exchange processes is highly tied to the wind speed. In high wind days, the ASL is well-mixed, properly coupled, and not a wave-guide for gravity waves. The conditions are homogeneous and quasi-stationary, turbulent fluxes are controlled by u_*, and therefore well understood through similarity theory. A properly established ASL, by the theoretical definition given in Chapter 1, is therefore present in high wind days. Conditions are more complicated during low-wind days (Mahrt et al., 2012; Anfossi et al., 2005). Without strong wind to control the ASL, weak, intermittent flows become dominant. Additionally, radiative cooling at the surface is not offset by the mixing down of warm-air aloft, resulting in the formation of surface-based inversions. A surface-based inversion provides a wave-guide for gravity waves, which are frequently observed in coastal Antarctica (Rees et al., 2000; Cava et al., 2015). As AWS5 is on a slope, inversions will result in a horizontal pressure gradient which will drive katabatic flows (Mahrt, 1982). The dynamics of slope flows further complicates the observed signal. Section 4.1 develops an understanding of wind meandering and distinguishes the phenomena between inertial and forced meandering. This is followed by case-studies and statistics on the occurrence of wind meandering at AWS5. Section 4.2 addresses katabatic flows, a prominent feature of the Antarctic atmosphere, and the main mechanism for the observed wind meandering.

4.1 Wind Meandering

4.1.1 Introduction to wind meandering

The ASL during low-wind conditions is observed to have wind meandering (WM), i.e. a high variability in the wind direction (Anfossi et al., 2005; Mahrt, 2007). What is responsible for the formation of WM is not completely understood (Vickers et al., 2008). The simplest mechanism for WM is the passing of meso-scale or submeso-scale motion. This can include, for example, gravity waves, density currents, and solitons (Mahrt, 2007). Meso- and submeso-scale motions are most prominent during low-wind days. In the following work, this form of WM is denoted as forced meandering (FM), which can be further categorized as persistent FM and intermittent FM. Intermittent FM are WM cases which occurs as isolated events, for example, the passing of a single soliton. In cases where the submeso-scale or meso-scale motions are long lived, the WM is best characterized as persistent FM. Intermittent FM can be associated to either individual disturbances propagating through the domain or full-layer instability, while persistent FM are from disturbances with a local generation mechanism. Persistent FM has been found, in certain cases, to be more common than intermittent FM in the ASL (Lang et al., 2018). It is important to note that FM is associated to turbulent intermittency. For FM, the evolution of the mean profile of a variable is considered, while turbulent intermittency is a property of the variance. As the mean and variance are couple, FM and turbulent intermittency are two sides of the same coin. This work will focus entirely on the FM perspective, though it is interesting to keep turbulent intermittency in mind throughout the results.

If FM explained the whole WM phenomena, low-wind conditions without the presence of meso-scale or submeso-scale motions would not have any WM. This is not the case and Oettl et al. (2005) proposed that WM is an intrinsic property of the atmosphere when a flow becomes two-dimensional, and does not require any trigger mechanisms. Theoretical studies by Goulart et al. (2007) showed that two-dimensional horizontal oscillations are an asymptotic solution to the 3D Navier-Stokes equations, when turbulent fluxes are assumed negligible. Such solutions have an infinite relaxation time, implying the existence of a lower-bound on the wind speed variance. This theoretical form of WM is denoted inertial meandering (IM). There is no direct proof that the asymptotic solutions are manifested in the real world, but for practical reasons, IM will be considered the oscillations in wind which resembles the theoretical oscillations described by Goulart et al. (2007).

During the three FINNARP campaigns (F10, F14, and F18), WM is a commonly observed feature of the ASL. The unique characteristics of the Antarctic ASL at AWS5 provides a new perspective on the generation mechanisms and properties of WM. Low-wind conditions are present during cases with weak synoptic pressure gradients, where the ASL is allowed to evolve freely and IM may be observed. During cloudless, low-wind nights, associated with a weak synoptic pressure gradient, the surface energy balance is negative which results in a surface-based inversion. This inversion taken on a slope will cause katabatic forcing which accelerates the flow, and the ASL can no longer freely evolve. In addition, if the katabatic forcing opposes the synoptic pressure gradient, low-wind periods will occur in the presence of forcing. WM under such conditions would fall under persistent FM.

To investigate WM, the theoretical formulation described in Anfossi et al. (2005) is followed.

WM is described through the EAF,

$$R(t) = \frac{\langle \xi(\tau + t)\xi(t) \rangle}{\sigma_\xi^2}. \tag{4.1}$$

An alternative option is to use wind constancy to categorize WM, this is a bulk method and will lose information on the WM, as well as miss periods with slowly evolving oscillations. In cases of WM, it has been noticed that the EAF of horizontal wind has a large negative lobe, i.e the autocorrelation has a well defined negative minimum (Anfossi et al., 2005; Oettl et al., 2005; Mortarini et al., 2016b). This negative lobe is a result to the negative correlation that occurs between half a period of an oscillation, further oscillation can remain coherent depending on the time scales of decorrelation due to turbulence. For this reasons, the theoretical EAF,

$$R_M(\tau) = e^{-p\tau} cos(q\tau), \tag{4.2}$$

is considered. The exponential term represents the decay of autocorrelation due to turbulence, while the cosine term represents the maintenance of autocorrelation due to WM. The turbulent and meandering time scales, T_T and T_M, are defined as follows,

$$T_T, T_M = \frac{2\pi}{p}, \frac{2\pi}{q}. \tag{4.3}$$

The ratio of q and p is called the loop parameter m by Mortarini et al. (2013) and represents the ratio between the meandering timescale and the turbulent timescale,

$$m = \frac{q}{p} = \frac{T_T}{T_M}. \tag{4.4}$$

The turbulent timescale (T_T) was chosen with a factor of 2π to simplify the above relation. In the limit where turbulence is dominant, i.e when $m \ll 1$, the first order approximation of the Taylor expansion of R_m will result in,

$$R_T(\tau) = e^{-p\tau}. \tag{4.5}$$

The turbulent timescale for the EAF, $R_T(\tau)$, is related to the turbulent integral timescale (T_{int}) as,

$$T_{int} = \int_0^\infty R_T(\tau) = \frac{1}{p}. \tag{4.6}$$

When $m > 1$, the flow can be considered WM dominant, as the timescale of the WM is smaller than the turbulent timescale.

In the following WM analysis, the velocity in each hour-long window was projected into streamline coordinates using the double-rotation method, see Chapter 2. The velocity aligned with the mean wind will be referred to as the streamline component, the horizontal velocity perpendicular to the mean wind will be referred to as the cross-streamline component. The turbulent and meandering parameters p and q are then estimated for each window using a non-linear least-square method. Unless otherwise stated, p and q are for the streamline component

4.1.2   A quick look into wind meandering

In this section, multiple case-studies are presented to develop an understanding on how the EAF will behave for different meteorological conditions. Figure 4.1(a) and (b), shows the wind direction, wind speed and EAF's for the 2 m CSAT3 during the morning of the 13th of December, 2014. The conditions leading up to this hour was weak winds, less than 5 m/s, which drops at 6AM. There was little to no stable stratification during the night. A weak wind and neutral night-time stratification is indicative of a cloud-cover controlled ASL. During the period of study, the winds were calm, with amplitude less than 1 m/s. The mean temperature was -8°C and the stratification was observed to be neutral in the lowest 10 m of the ASL. The wind direction clearly shows a regular counter-clockwise rotation. The EAF of the streamline component demonstrates a large negative lobe, with minimum autocorrelation of -0.63 at 1250 s (20 minutes). The cross-streamline EAF shows a similar minimum, and the temperature shows no negative lobe. By curve-fitting the EAF to Equation 4.2, the turbulence and meandering timescale are 3.5 h and 0.7 h, respectively, resulting in $m = 5$. This case study has ideal conditions for IM as it has very low winds, and no stratification due to the cloud cover. It is characterized as being IM since both streamline and cross-streamline components have a similar minimum for the negative lobe of the EAF.
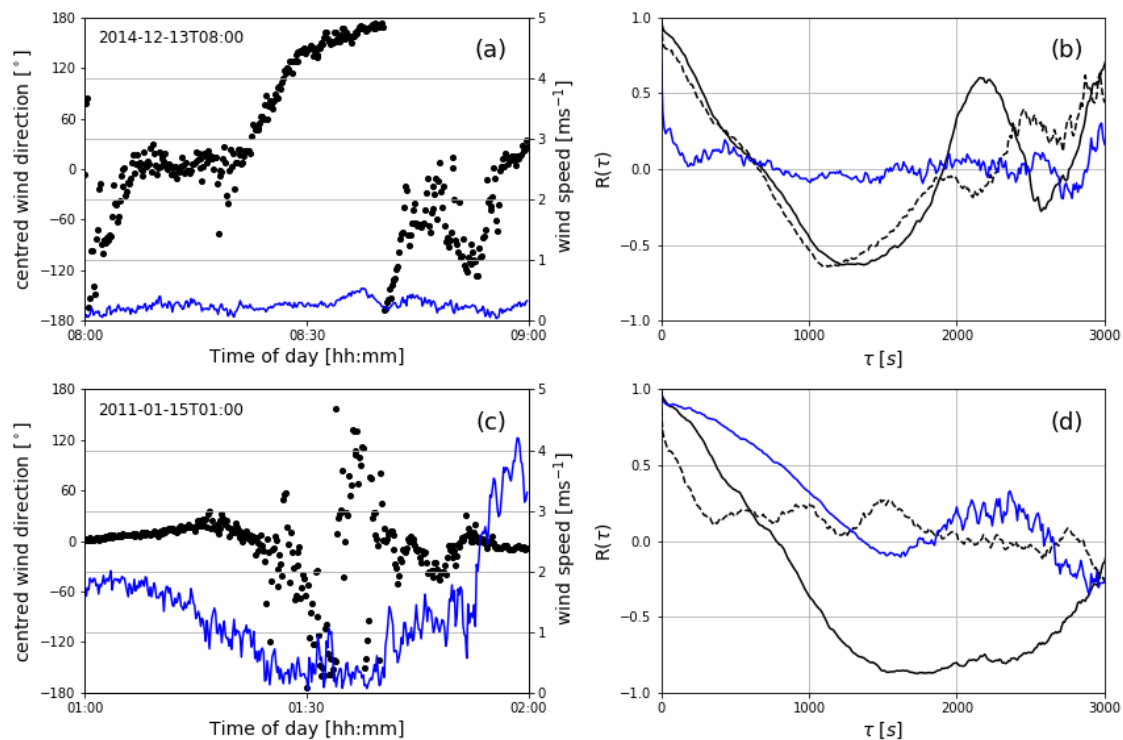

Figure 4.1: Panels a) and c) are the time series of the horizontal wind speed and the deviation of the wind direction from the hourly mean. Panels b) and d) are the the EAFs for the streamline component (black solid line), cross-streamline component (blacked dashed line) and temperature (blue solid line).

A second, contrasting case-study, is shown in Figure 4.1 (c) and (d). This case-study is from the 10 m CSAT3 during the 16th of January, 2011, in the middle of the night. Unlike the previously described case, the flow had a complicated character. The wind speed in the evening was below 1 m/s and increases with the start of the katabatic forcing, due to the formation

of the nighttime inversion. The wind-maxima is below 10 m during the development of an surface-based inversion, which reaches an 8° temperature difference between 2 m and 10 m. At 1:00, the 10 m wind speed starts dropping and is followed by a mixing event which destroys the surface-based inversion. During this hour, the 10 m wind meanders as seen in panel (c). After the mixing event, the stratification is re-established and the 10m wind re-accelerates with constant wind direction. WM of this kind is intermittent FM of a dynamic origin. The EAF's shown in panel (d) is less concise than the previous case. The EAF of the streamline component shows an extremely strong negative lobe, reaching -0.87 at 1500 s (25 minutes).The cross-streamline component does not exhibit WM but the temperature EAF does with a similar, yet weaker minimum than the streamline EAF. The meandering and turbulent timescales are 1.1 h and 62 h, respectively. The large turbulence timescale is due to its intermittent nature. During rapid mixing events in stable conditions, turbulence does not have time to adjust into a near-equilibrium state and therefore cannot decorrelate the signal in the same way it would during a fully turbulent regime.
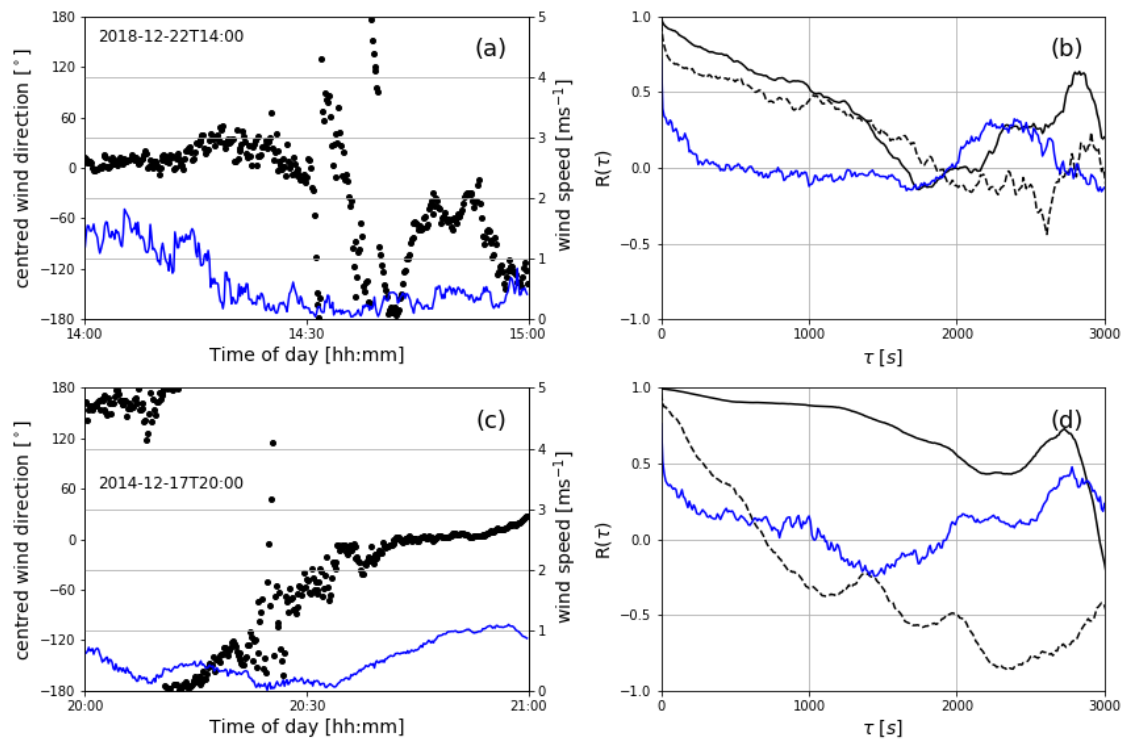

Figure 4.2: Panels a) and c) are the time series of the horizontal wind speed and the deviation of the wind direction from the hourly mean. Panels b) and d) are the the EAFs for the streamline component (black solid line), cross-streamline component (blacked dashed line) and temperature (blue solid line).

In addition to the rather illustrative case-studies in Figure 4.1, two other cases are discussed in order to establish some of the weaknesses in considering the hourly EAF's, and the resulting p, q, and m parameters. The first is seen in Figure 4.2(a) and (b). The wind speed is initially around 1.5 m/s but drops for 15 minutes right before 14:30, with an slightly increasing tendency afterwards. Even though it is a small time span with near zero wind speed, WM is immediately present as seen in panel (a). When computing the EAF for this period, the negative lobe structure is masked by the high autocorrelation of the periods in the hour with

higher wind speeds. Characterizing WM from hourly averaging, as done in many studies including this one, will lose WM events. Any statistical analysis of WM is sensitive to the choice of the averaging window.

Secondly, panels (c) and (d) shows a case where the 10 m wind is rotating slowly in time, and gradually increases after 20:30. This occurred during the evening transition, where conditions were changing to a night-time katabatic flow, and is therefore FM. The minimum of the streamline EAF is -0.7 and the value of m is 4.4, giving a false impression of the existence of a strong negative lobe. In reality, the streamline EAF shows an irregular structure. Many hour long intervals have irregular EAF structures which are not nicely described by Equation 4.2, putting in question the validity of this approach.

4.1.3   Regimes of wind meandering

In the previous section, only one hour windows were investigated for different cases exhibiting WM. This is not a coincidence as the statistics of WM, for the *AA-MET-TURB* data set, will be calculated using hour long windows. This window choice has the disadvantage of losing shorter periods with WM, but no logical alternative was conceived. For every one hour window in the *AA-MET-TURB* data set, the parameters p, q and m are computed using Equation 4.2 for the streamline component. Figure 4.3(a) shows the distribution of m. There is a bimodal structure with isolated distributions for cases where $log(m) \in [-6, -3]$ or $log(m) \in [-1, 2]$ referred to as the δ_{-5} and δ_0 distributions, respectively. There are no m such that $m \in [0.001, 0.1]$. This result is rather surprising. This inequality states that if T_T is more than one order of magnitude smaller than T_M, then it is at least three orders of magnitude smaller. There are two explanations for this rather counter-intuitive result. The physical explanation is that there is a coupling between WM and turbulence, i.e not linearly superpositioned in the time-series. A second explanation is the nonlinear regression method fails due to the orders of magnitude variability in the data. The nonlinear regression used is the Levenberg-Marquardt algorithm through the python package *scipy.optimize*. It is most probable that both physical and numerical features are contributing to the observed results, the following analysis will address both simultaneously.

Values of $q < 10^{-4}$ are responsible for δ_{-5}. The magnitude of q values are pushing the validity of the regression method, but also represent oscillations larger than the timescales of interest, or a lack of oscillations altogether. In terms of the regression, EAFs which are members of δ_{-5} are represented by R_T, resulting in high uncertainty in q. There is no strict cutoff in the q distribution, as seen in panel (b), implying a continuous shift into a region of high uncertainty. For values of $q < 10^{-4}$, the 1 hour window is not long enough to contain precise information on those timescales. Furthermore, the transition near 10^{-4} is also populated by values of p, implying that they may be coupled and members of δ_0. To consider the relationship between T_T and T_M, they are plotted against each other in Figure 4.4. The fact that T_M is of high uncertainty in the $q < 10^{-4}$ regime does not influence the distinct nature of the δ_{-5} and δ_0 distributions. The bimodal structure is clearly seen in 4.4. The linear relationship between T_T and T_M observed for δ_0, seen here in the lower right, is most likely a product of the numerical algorithm implemented in the regression. What is physical is the property that short T_M are associated with long T_T. The $m = 1$ line is plotted in black, a majority of the points in the δ_0 distribution are above the line. When considering WM, Mortarini et al.

(2016b) chose the cutoff criteria as $m > 1$. From both Figure 4.4 and Figure 4.3 an alternative criteria which is used from now on is to isolate WM through $m > 0.01$ (the dashed black line in Figure 4.4). Choosing $m > 0.01$ results in the same categorization as choosing WM cases through $q > 10^{-4}$ (the dashed blue line in Figure 4.4). The WM cases consist of 34% of the intervals. It is important to note that WM as defined by $m > 0.01$ is very broad and encapsulates intervals with very little oscillatory behaviour. The value of keeping the term WM vague is that no arbitrary choice was made. Motions that are classified as FM can be of very different origin, and cover a wide range of m values, while IM is more particular and harder to isolate.

To further explore the behaviour of m, Figure 4.5 shows the relationship between m and the local mean and turbulent quantities, computed at the 2 m level for each 1 hour window. The TKE, ζ, $\overline{w'T'}$, and wind direction shows no distinguishing features relating to the two distributions of m. Perhaps one could say that stronger negative values of covariance between temperature and vertical velocity is associated with smaller m values, but it is by no means definite. A more promising relationship is that higher wind speeds and larger u_* are associated with lower m values. An increase in u_* does theoretically cause decoupling of the two horizontal components breaking the undulating behaviour of IM (Goulart et al., 2007). Perhaps this is a result that can be generalized for all wave-like phenomena in the ASL. Unfortunately, wind speed and u_* cannot be used as a criteria to distinguish between δ_{-5} and δ_0.
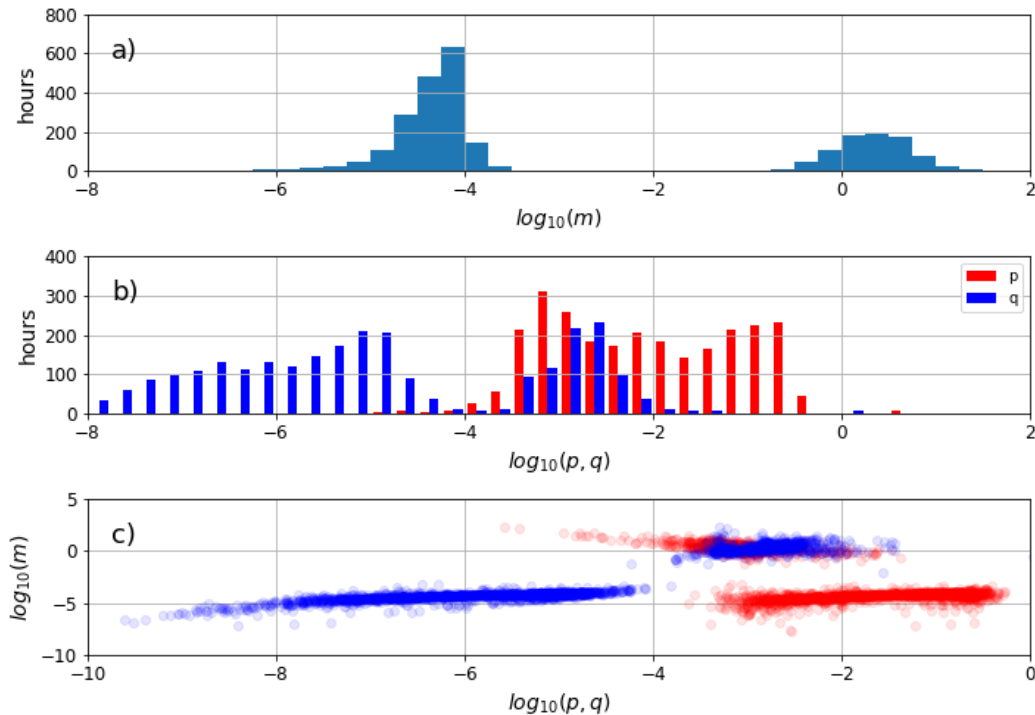

Figure 4.3: Curve-fitting the EAFs to Equation 4.2 for the 2 m CSAT3 data for the full AA-MET-TURB data set. (a) Histogram of m. (b) Histograms for p and q, (c) m as a function of p and q.
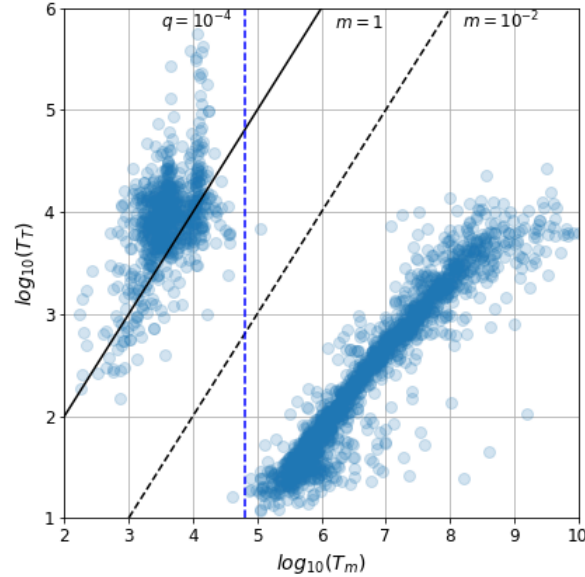
Figure 4.4: Turbulent timescale (T_T) vs. the meandering timescale (T_m). Additionally, the $m = 1$, $m = 0.01$, and $q = 10^{-4}$ lines are drawn in black solid, black dashed, and blue dashed, respectively.

It is useful at this point to develop a thought experiment that determines possible physical relationships between m, p, and q. In a region where turbulence is very strong, any wave-like phenomena moving through the area will lose its coherence and therefore its identity, resulting in no propagation. This purely annihilation process would see any wave-like phenomena disappear and $m \approx 0$. The δ_{-5} distribution could be in part that regime and in part a regime where no wave-like motions are present. This is the crux of the problem, there are no ways of distinguishing regions where the turbulent signal is consisting of just locally generated turbulence or if it is also reinforced by non-local energy caused by wave-breaking. In cases of wind speed greater than 10 m/s, there are no oscillatory cases belonging to δ_0. Perhaps this is due to masking the signal though it seems more likely it is a property of the ASL. Either way, event based phenomenology is not captured in either the mean or the turbulent statistics so the lack of evident dependency in Figure 4.5 is not surprising. The lack of values of $m \in [0.001, 0.1]$ does support the hypothesis that there is a critical value of ASL turbulence where no wave-like phenomena can exist. This is independent of the uncertainty in the computation of q. The ASL in that regime is a near-perfect sink of meso-scale and submeso-scale energy.

The next consideration is the diurnal cycle of WM. Due katabatic forcing, there is a diurnal cycle in the forcing mechanisms which could result in a diurnal cycle of the occurrence of WM. This is plotted in Figure 4.6(a), which shows a gentle diurnal cycle with the minimum around noon and maximum in the late evening. Taking it one step further, panel (b) shows the persistence of WM in relation to the time of day. A period of WM is considered persistent if the previous and following hour intervals are also classified as WM. The diurnal cycle of persistent WM is more aggressive than for WM as a whole, with a maximum in the evening between 20:00 and 22:00. The minimum is found at 14:00, where only 4 hour intervals were found to have persistent WM in the whole *AA-MET-TURB* data set. Due to the number of sample intervals, over-interpreting smaller features in the distribution is risky, as the statistical significance is low. Figure 4.6 supports the hypothesis that WM is largely due to katabatic forcing at AWS5.
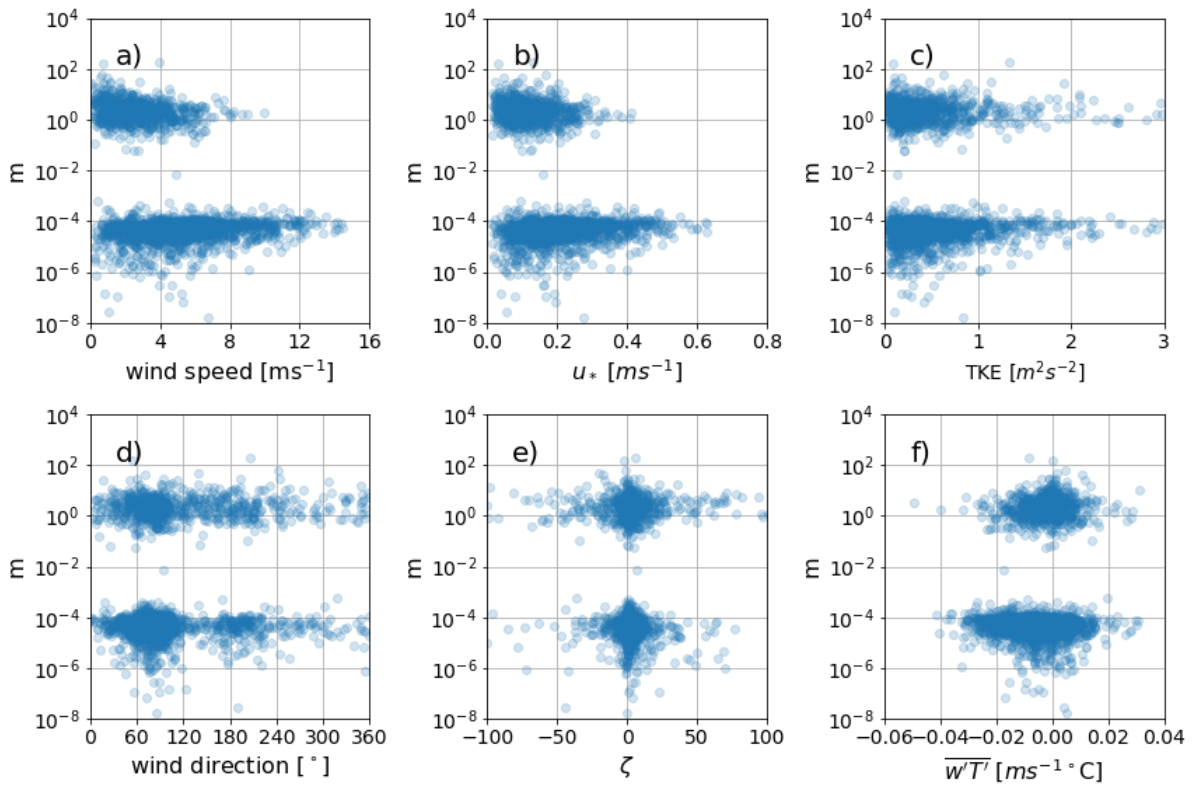
Figure 4.5: The dependency of m on a) wind speed , b) friction velocity, c) TKE, d) wind direction, e) stability parameter and f) kinematic heat flux.
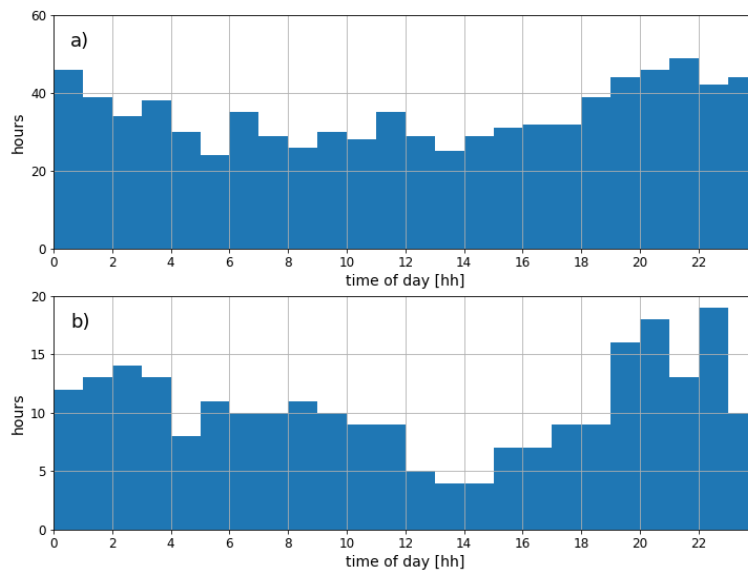

Figure 4.6: Diurnal cycle of WM occurrence. a) is the diurnal cycle for all WM, b) is the diurnal cycle for persistent WM.

As of yet, only the q parameter for the streamline component is considered in the analysis of WM. Figure 4.7 shows the relationship between the streamline and cross streamline components, as well as with vertical velocity, and temperature. The parameters are displayed in terms of the periods of oscillation, i.e $2\pi/q$. From panels a) and c), WM in the streamline component is associated with WM in both the cross-streamline component and the temperature. The latter is more interesting as it is not obvious from the two dimensional mode that is often visualized when considering WM. Mortarini et al. (2016a) reported similar features in observations from the urban environment of Turin, as well as over the amazon forest in Brazil. The oscillations in temperature were hypothesized to be due to horizontal temperature gradients. This should not be the case around AWS5, due to the horizontal homogeneity. More complicated physics are at play. The temperature oscillations may be due to horizontal convergence and divergence of the wind-field modulating the temperature field through vertical perturbations. Panel b) shows that the vertical velocity oscillations exist on different scales to the horizontal wind and temperature. The vertical velocity EAFs are dominated by small scale features and may not be representative for the flow behaviour.
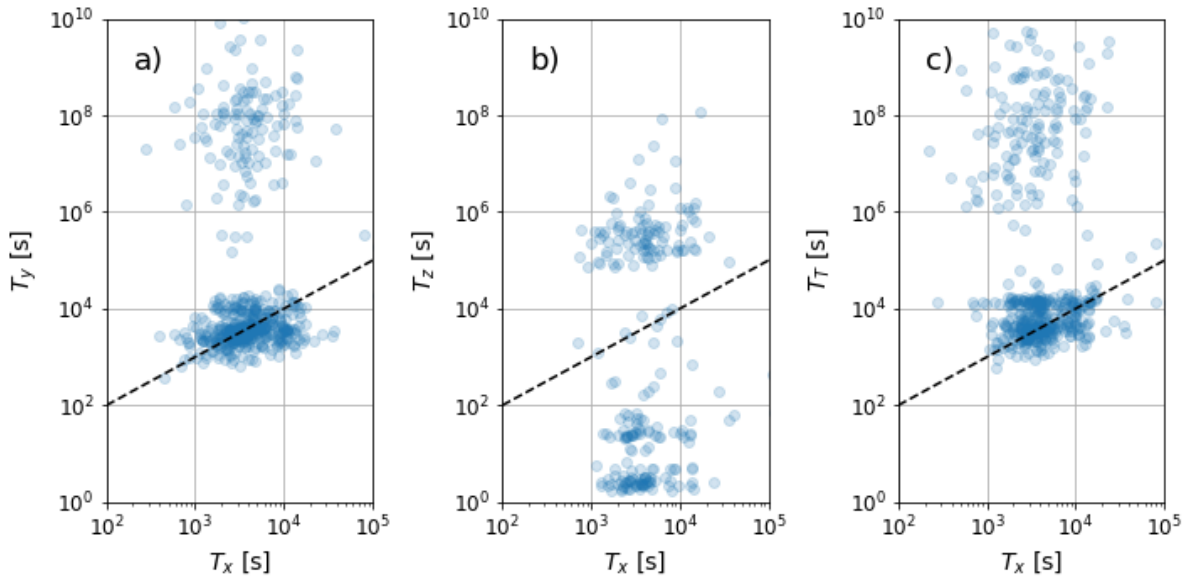

Figure 4.7: The relations between the meandering timescale of the cross-streamline component (T_y), vertical velocity (T_z), temperature (T_T) to the meandering timescale of the streamline component (T_x).

4.2 Katabatic Flows

4.2.1 Introduction to katabatic flows

The most prominent feature of the Antarctic atmosphere is the katabatic wind. The katabatic wind is the strongest and most persistent wind observed on the planet. Cape Denison in Adélie Land has an annual mean wind speed of 20 m/s (Wendler et al., 2004). As extraordinary as this may be, it is not representative of the whole Antarctic continent and to understand the Antarctic surface climate and circulation, all regimes should be investigated.

Katabatic flows (KFs) can be considered through a local and/or non-local perspective, similar to the Eularian and Lagrangian formalism, respectively. A KF with properties which

adhere to one perspective better than the other will be denoted as such. In reality, KFs have properties due to both non-local and local effects. Non-local KFs are gravity currents advected into the domain. This primarily occurs when the surface of the Antarctic plateau cools due to a negative energy balance, available potential energy is accumulated and is eventually released in the form of a drainage flow. The drainage pattern over the continent is a three-dimensional problem and analysis of longitudinal slices of the orography is too idealized to explain the observations. The persistence of wind in certain regions of coastal Antarctica is due to convergence in the streamlines of the drainage pattern. Those areas are referred to as confluence zones and have a nearly unlimited supply of cold air during the winter (Parish and Waight, 1987; Parish, 1982). Equilibrium is only achieved due to this unlimited supply and in general non-local KFs are unsteady. The time-dependent aspects of the non-local KFs are only in magnitude and not direction, as KFs in Antarctica are orographically controlled. Furthermore, even without radiative cooling, Antarctic wind would have a very high directional constancy due to its continental geometry. Observations of directionally constant wind can be misinterpreted as katabatic when it is in fact synoptically driven (Parish and Cassano, 2003). The presence of low-pressure systems north of the ice-edge modulates the strength of KFs by creating a demand which is met by the supply of cold air residing over the Antarctic plateau (Parish and Bromwich, 1998). The KFs time evolution is dependent on the position of the low-pressure systems in relation to confluence zones, therefore the strongest flows occur when the synoptic pressure gradient reinforces the katabatic forcing. The presence of polynyas can also reinforce KFs (Savijärvi, 2011). Non-local KFs are understood by tracing the origins of the cold air masses and their driving mechanisms.

Local KFs are formed through the radiative cooling of air over a slope, where the surface energy balance is controlling the flow. The dynamics then follow the classical mechanisms of a KF where the flow is forced by the horizontal pressure gradients due to a surface based inversion. Theoretically, local KFs are well expressed in terms of longitudinal slices of the orography making it a quasi two-dimensional problem. The properties of local KFs are highly dependent on the slope angle. For steep slopes the balance is between the pressure gradient and the surface stress, and for gentle slopes the balance is between the pressure gradient and the Coriolis force (Mahrt, 1982). The latter implies that the flow is nearly perpendicular to the fall line. These features may also hold for non-local KFs.

When determining the surface climate of a specific area, both local and non-local perspectives should be considered as well as thermodynamic and dynamic processes. Fluid parcels following the drainage trajectories moving from one geographically area to another have hysteresis but also evolve following the local energy balance and mixing. The adjustment timescale of a parcel to local conditions is key to understanding the role KFs have on the local meteorological conditions, specifically temperature and humidity. KFs have been observed to both decrease (Periard and Pettre, 1993) and increase (Streten, 1990) the temperature in the ASL. Using two-dimensional numerical modelling, Vihma et al. (2011) showed that potential temperature decreases along the fall line due to accumulation of cold air at the foot of the slope. This is a climatological feature of the Antarctic circulation as the air parcels with low potential temperature are replaced by subsidence of warm subantarctic air (Parish and Bromwich, 1997). This lapse rate is reversed during strong KF events, as warm air aloft is mixed down due to the sensible heat flux forced by the KFs.

With only point sources of data, it is impossible to formally distinguish the KF regimes observed at AWS5 but with consideration of the above discussion, it is possible to make infer-

ences. The wind at AWS5 has a climatological direction almost perpendicular to the fall line. As such, if there are local KFs, the balanced is between Coriolis and the inversion pressure gradient. If a KF has a maximum wind speed much higher than 10 m, it is indistinguishable to the ASL from a synoptically driven wind. Considering the two indistinguishable at AWS5 is particularly valid, as the mean katabatic and synoptic pressure gradient forces are aligned. Even with higher resolution vertical sampling, the upper level winds around AWS5 are governed by complicated interactions between katabatic and synoptic flows which cannot be distinguished from observations alone (Kouznetsov et al., 2012). The presence of strong upper-level flow of any origin will erode any surface based inversions and remove any local, low-level katabatic forcing. Under such conditions the ASL loses much of its complexity.

4.2.2   Katabatic flow statistics

As the consideration of this work is on the ASL, the KFs are considered in cases where there are surface-based inversions. This criteria suits its purpose, as katabatic forcing occurs when the surface-based inversions are not eroded. The temperature and velocity differences between 10 m and 2 m will be denoted by $\Delta\overline{T}$ and $\Delta\overline{U}$, respectively. To avoid the scatter associated with near-neutral stratification, and cases with negligible katabatic forcing, the cutoff chosen for a thirty minute interval to be considered katabatic is a $\Delta\overline{T}$ value of at least $1\,°C$,

$$\Delta\overline{T} = \overline{T}^{30}_{10m} - \overline{T}^{30}_{2m} > 1°C. \tag{4.7}$$

Criteria 4.7 was met for 27%, 17%, and 32% of 30 minute intervals for the F10, F14, and F18 campaigns, respectively. Figure 4.8 shows the diurnal cycle of occurrence of KFs as well as the distributions of $\Delta\overline{T}$ and $\Delta\overline{U}$. The occurrence of KFs exhibits a well defined diurnal cycle with the start and end at 18:00 and 10:00, respectively. The highest occurrence of KFs is between 23:00 and 1:00 with a surprisingly linear decrease of occurrence on either side. During the formation stage, between 18:00 and 23:00, the linear trend shows an increase in occurrence of 16 intervals per hour. During the dissipation stage, between 1:00 and 10:00, the linear trend shows a decrease in occurrence of 9 intervals per hour. This result is counter to the commonly observed feature at mid-latitudes, that the development of inversions in the evening is slower than the development of a mixed-layer in the morning. Consideration of the ground heat flux term in the surface energy balance may explain the difference, but it is beyond the scope of this work. Alternatively, the synoptic conditions required for the occurrence of long-lived surface-based inversions may be responsible for the trends, as opposed to the surface dynamics. Long-lived inversions are therefore not a commonly observed feature of the ASL as non-climatological winds are required. This is confirmed in the distributions of the temperature and wind speed gradients (panel b and c) where a majority of the 30 minute intervals exhibit gradients of 1 to 2 ° C and 1 to 2 m/s for temperature and wind speed. Comparing the diurnal cycle of KFs and persistent WM (Figure 4.6), the hours with the highest occurrence of persistent WM are right before and after the maximum in KF occurrence. This supports the hypothesis that persistent WM occurs in the development and dissipation of KFs. The maximum temperature inversion is $\Delta\overline{T} = 8.8\,°C$ and a wind speed inversion with $\Delta\overline{U} = -2.1\,m/s$. The strongest wind speed inversion is underestimated, as the low-level maxima may be higher than 2 m.
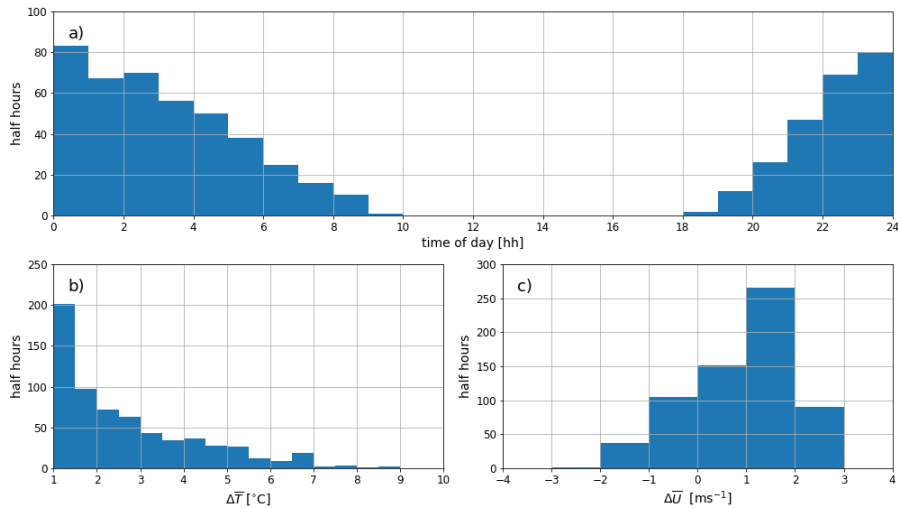
Figure 4.8: Panel (a) is the diurnal cycle of surface katabatic flow occurrence. Panels (b) and (c) are the histograms of $\Delta\overline{T}$ and $\Delta\overline{U}$, respectively

The 2 m level will be considered the canonical level for low-level katabatic flows. To study how the wind speed at 2 m is related to the inversion strength, Figure 4.9(a), shows the 2 m wind speed as a function of $\Delta\overline{T}$. With increasing stratification there is a decrease in the scatter of the wind speed, this may be due to under sampling of strong inversions. The mean 2 m wind speed (black line) averages around 3.5 m/s with a slightly increasing tendency with increasing inversion strength. The wind direction, as seen in panel (b), is from the east during KFs therefore the leading mode of low-level, local KFs is [80°, 3.5 m/s]. This mode is consistent with one of the leading modes of the mean wind conditions in Figure 3.6. Both the F10/F18 and F14 exhibit this weaker wind speed mode as well as a second mode from the same direction but with a stronger wind speed. To determine weather or not multiple synoptic modes cause these maximums and minimums, or if it is in fact the katabatic mode, would require further investigation into reanalysis data.
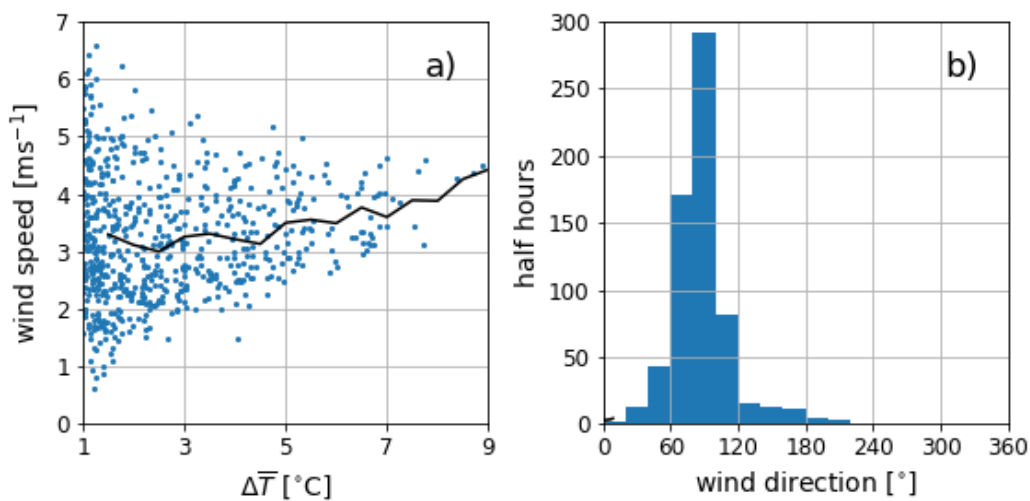

Figure 4.9: Mean wind conditions during periods with surface-based inversions. a) The 2 m wind speed vs. $\Delta\overline{T}$. The black line is the bin-averaged mean. b) the distribution of wind direction.

4.2.3   The formation, balancing, and dissipation of katabatic flows

To develop an understanding on the KF regimes at AWS5, five case-studies are presented in Figure 4.10. The synoptic forcing due to synoptic pressure gradients are represented through the pre-inversion wind speed and wind direction. The first case-study (panels a, b and c) is a case with a weak synoptic forcing. The initial wind comes from 110° and therefore partially aligned with climatological wind which includes KFs, as seen in Figure 4.9. With the formation of an inversion at 19:00, the wind speed gradually increases with increasing inversion strength. By 23:00, the temperature difference between 2 m and 10 m is 6° C and the 10 m wind speed starts dropping. This is indicative of a change in the synoptic conditions. The competition between the katabatic and synoptic forcing results in the meandering of the 10 m wind, this is a common feature of the effects of low-level KFs at AWS5. The shear associated with the WM forces locally generated turbulence resulting in the observed variability in the 2 m temperature. The temperature variability ends around 7:00 which is coordinated with the end of the WM. The 10 m wind speed re-accelerates to the 2 m level and the inversion dissipates gradually in the morning following the diurnal cycle. The second case-study (panels d, e, and f) is similar but with the initial wind coming from 180°. The inversion starts at 20:00 and similar to the first case-study, the wind-speed accelerates and shifts to 90°. The temperature difference between 2 m and 10 m reaches 7° C. At 1:30, the 10 m wind speed drops and the full layer overturns. Interestingly, after the overturning event, the flow adopts an equilibrium profile with little to no variability for over three hours. Both the 2 m and 10 m wind speed drop with the end of the katabatic forcing at around 5:00 and the inversion is dissipated. The WM that occurred during the overturning event was explored in Section 4.1.2, Figure 4.1. The third case-study (panels g, h, and i) has an initial wind from 300°, directly opposing the katabatic flow. The inversion starts at 19:00 resulting in an increase in 2 m wind speed. There is a delay in the rise of the 10 m wind speed as the synoptic pressure gradient must be overcome. A higher wind KF is persistent around 3:00 with a 2 m/s bulk shear between 10 m and 2 m. After the weakening and end of the katabatic forcing the wind shifts back to the evening wind direction of 300°. The last two case-studies show more complicated time-series without clear interpretations. The fourth case-study (panels j, k, and l) is similar to the second with an overturning event after a drop in the 10 m wind speed. The wind is stronger, and of a more complicated nature. After the overturning, the wind is re-established to a different direction altogether. It is fair to consider this case as a complicated mix of interacting processes. The last case-study (panels m, n, and p) exhibits very odd oscillatory behaviour. The 2 m wind speed variability has an amplitude of 3 m/s with associated wind direction shifts and aggressive WM at the 10 m level. This could be interpreted as a pulsing katabatic flow (Doran and Horst, 1981; Mahrt and Larsen, 1982) which under our categorization is a non-local KF. Further analysis into this flow is beyond the scope of this work.

The development of a KF is dependent on the initial synoptically driven wind. The first three case-studies have initial wind from 120°, 180°, and 300° respectively. In all cases, the 2 m wind speed increases with the start of katabatic forcing. When the synoptic gradient counteracts the katabatic force, the 10 m katabatic wind has a delayed onset and a low-level wind maxima occurs. Once the KFs are developed, changes in the synoptic gradient is the probable source of variability but non-local KFs may increase variability as well. Such variability can drive the observed 10 m WM which results in turbulence and in more aggravated cases, full
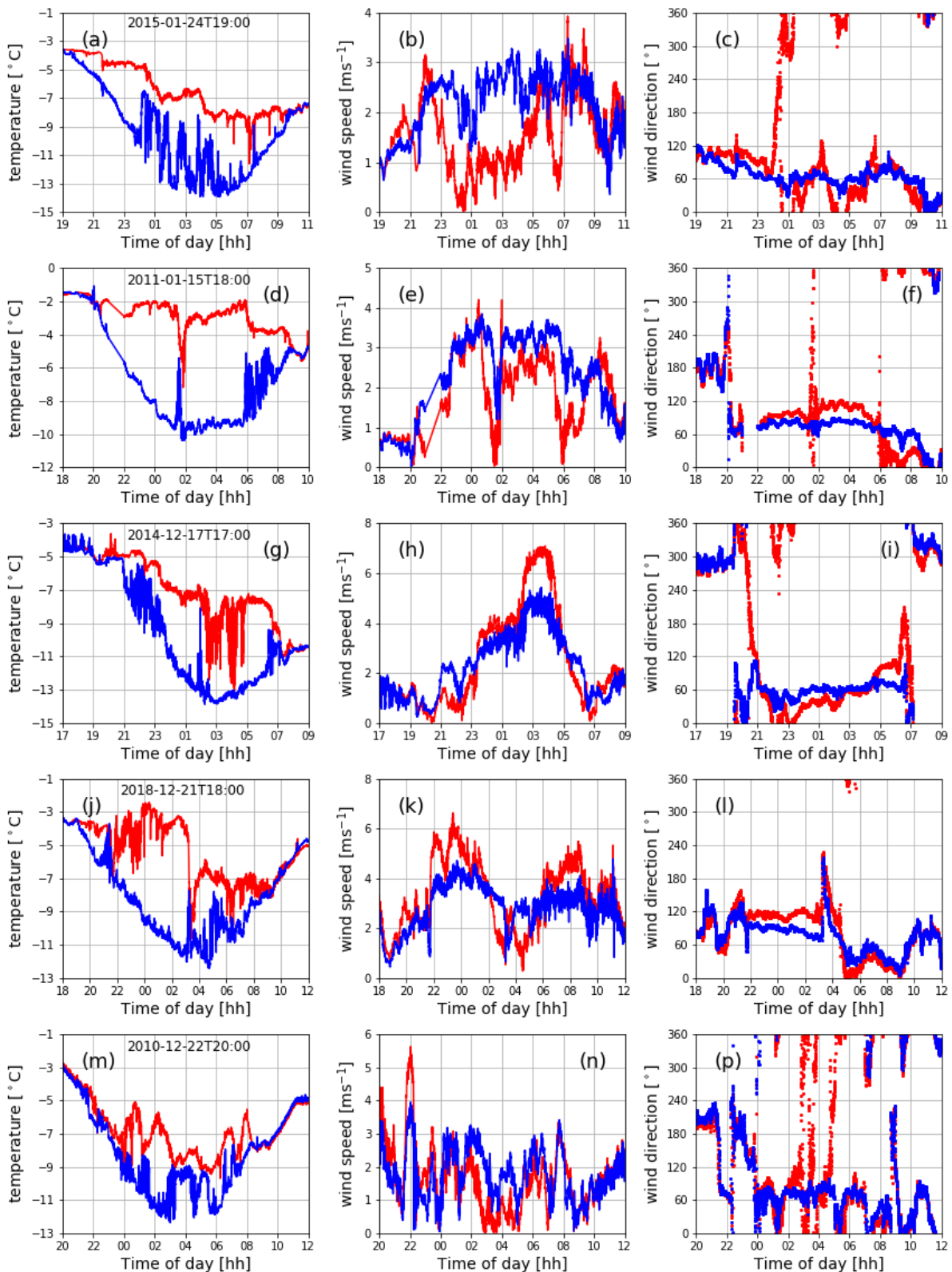
layer overturning.

Figure 4.10: Each row corresponds to a case-study of a KF. The 10 m data is in red while the 2 m is in blue. The date and time of each case-study is written in the first column.

In the first case-study, the vertical shear generated small-scale turbulence causing continuous

mixing while in the second case-study the shear overturned the whole layer. The transition between those two contrasting regimes is known as the hockey-stick transition (HOST) and has been discovered in turbulence statistics (Sun et al., 2012; Mahrt et al., 2012). If winds are weak, the turbulence scales to the local shear, while if the winds are strong enough, the turbulence scales to the bulk shear. It is important to note that HOST generally considers the bulk shear from a given level to the surface, while in this case it is the inverted shear as a result of a low-level maxima that drives the instability. In both the first two cases the 2 m wind speed was stronger than at 10 m. This does not hold for the third case-study when the synoptic gradient directly opposes the katabatic forcing. The strongest katabatic winds from the 90° sector occur when the synoptic flow is from 300°. This counter-intuitive result can be explained through cold-air accumulation. As the 10 m wind speed has the longest delayed onset during the third case-study, the synoptic wind blocks the downward moving cold-air resulting in its accumulation. When the synoptic gradient is no longer capable of restraining the katabatic flow, the strongest katabatic wind speeds were observed. Such a mechanism was considered in Mahrt (1982), where counter-synoptic, front-like katabatic flows were observed. In cases where the synoptic wind is from 90° with wind speeds around 5 m/s, the 10 m wind speed is larger than at 2 m throughout the night. The local KFs are therefore not dominant yet the synoptic wind is not strong enough to erode the inversion. Such cases are simpler in physics and should be well represented by similarity theory.

Chapter 5

The Structure of Turbulence in the ASL

This chapter addresses the structure of turbulence in the ASL. The following adopts the hypothesis that turbulent fluxes are scaled by the local shear. The formulation of MOST is built off this assumption, but current work is questioning its validity (Sun et al., 2012; Mahrt et al., 2015). Through the HOST, introduced in Chapter 4, under strong winds, turbulence is more appropriately scaled the the bulk shear than the local shear. Further analysis into HOST is warranted, but beyond-the-scope of this work.

Regimes of turbulence are often characterized through the stability parameter (ζ) defined in Equation 1.11 (Businger et al., 1971; Högström, 1988; Grachev et al., 2005). Negative values of ζ represent an unstable ASL, and are not considered in this work. The larger $\zeta > 0$, the more stable the conditions are. This interpretation of ζ loses meaning for large values, where the pointwise measurement of ζ is no longer a representative parameter of the ASL. The balance in ζ is between the heat flux ($\overline{w'T'}$) and the friction velocity (u_*), which is often forced by the mean wind. As u_* is cubed in the denominator, errors in the computation of u_* can erratically change the values of ζ. This error is prominent during regimes with small values of u_*. The structure of ζ is presented in Section 5.1. Once ζ is put into context, the validity of MOST is investigated in Section 5.2. As the stability regime of interest is weakly stable to stable, MOST is expressed in terms of Equation 1.19. Differences between the temperature and wind speed similarity relations are examined through the turbulent Prantl number (Pr_t). As the assumptions of MOST fail under conditions of wave activity, the influence of the loop parameter m, from Section 4.1, on the validity of MOST is investigated in Section 5.3.

In this chapter, the different years are usually considered separately, as alignment errors and other data features are different for the data sets. Combining the errors will confuse the interpretation of the results. For details on the eddy-covariance and gradient calculations, see Chapter 2.

5.1   The Structure of Stability

The distribution of ζ is shown in Figure 5.1 for the F10, F14 and F18 campaigns. The three campaigns have similar distributions of ζ, summarized through Table 5.1. Unstable conditions with $\zeta < 0$ occurs on average, 29% of the time, with F18 exhibiting less unstable days than the previous two campaigns. This difference is also reflected in the $0.1 < \zeta < 1$ range which is more populated for F18. The near-neutral/stable regime, $0 < \zeta < 0.1$, was similar for all campaigns with a mean occurrence of 49%. This regime is therefore the most com-

monly occurring regime at AWS5, a promising result as it is the range where Equation 1.19 is formally valid (see Section 1.2).
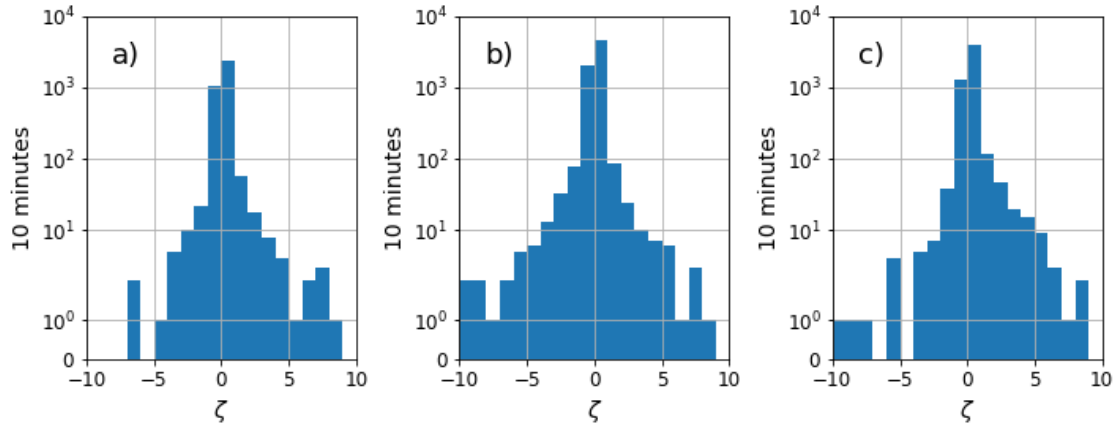

Figure 5.1: Distributions of the stability parameter , for a) F10, b) F14, c) F18.

Table 5.1: Occurrence of stability classes for the full AA-MET-TURB data set.

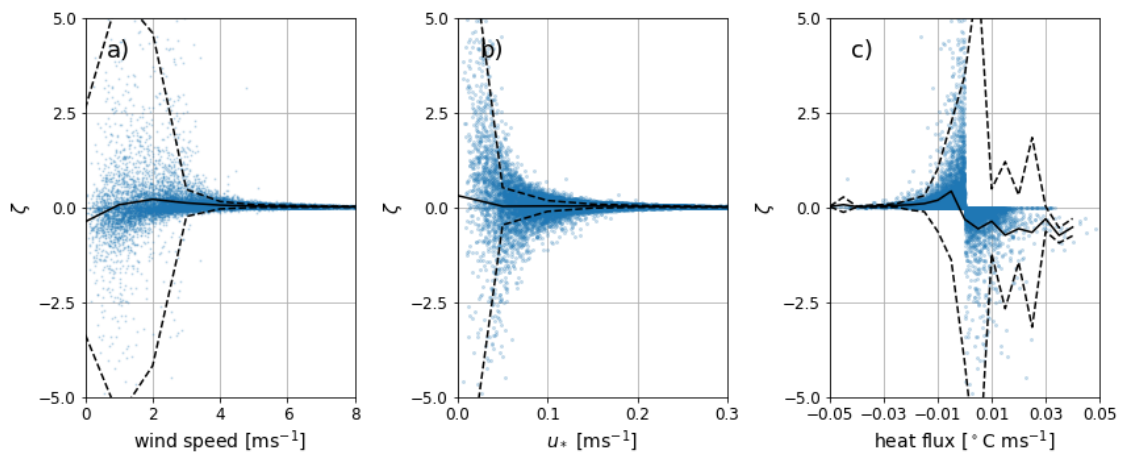| AA-MET-TURB			
	F10	F14	F18
$\zeta < 0$	31%	31%	25%
$0 < \zeta < 0.1$	49%	52%	47%
$0.1 < \zeta < 1$	17%	14%	24%
$1 < \zeta$	3%	3%	4%

Figure 5.2: ζ as a function of a) windspeed, b) u_*, and c) $\overline{w'T'}$. The solid black line is the mean, the dashed is the mean $\pm$ SD.

Figure 5.2 shows the dependence of ζ on the wind speed, u_*, and $\overline{T'w'}$. The wind direction (not shown) does not show any interesting features and is therefore not a controlling factor for the stability. This is not a surprise considering the horizontal homogeneity around AWS5. For wind speed above 5 m/s, the conditions are always near-neutral. Turbulence generated by

the horizontal wind shear provides ventilation for the surface during sunny days and erodes inversions during the night. This is also reflected in u_* where the critical value is 0.2 m/s. From Figure 5.2, the relationship between ζ and wind speed, and ζ and u_* are similar. This is investigated further in Figure 5.3(a), which plots u_* as a function of wind speed. When the wind speed is larger than 2 m/s there is a linear relationship with u_* with slope of 1/25. The slope value is dependent on the surface roughness length (z_0). In the limit of zero wind speed, u_* does not converge to zero. This is due to FM as discussed in Section 4.1. The binned mean of u_* shows a transition, between a constant and linear regime, at 1.5 m/s similar to the hockey-stick transition (HOST). If this is the same transition as discussed in Sun et al. (2012) and Mahrt (2014) is not clear and will not be discussed further. The relationship between the $\overline{w'T'}$ and ζ, Figure 5.2(c), is complicated by the presence of katabatic flows. Due to the slope, an increase in stratification will result in an increase in wind speed due to katabatic forcing. This will then result in larger values of u_* as established in Figure 5.3. Figure 5.3(b), shows the coupling between u_* and $\overline{w'T'}$. With an decrease in $\overline{w'T'}$, there is an initial decrease followed by a rapid increase in u_*. The minimum is located around $\overline{w'T'} = -0.05°Kms^{-1}$. This minimum is also seen as a maximum in Figure 5.2(c). The mean stability reaches a maximum value of around $\zeta = 0.5$. The implication of this result is that the ASL over a slope has a maximum achievable ζ. Another important consequence of this maximum is that in Figure 5.2, the largest values of ζ occur for very small $\overline{w'T'}$ and u_*. This is most likely erroneous and a product of the eddy-covariance calculations. Any data points with $\zeta > 1$ should be taken critically. Figure 5.3(b) shows that a functional dependence can only exist as $u_* = u_*(\overline{w'T'})$ and not vice-versa. This also holds for wind speed due to the linear relationship between wind speed and u_*. This implies that $\overline{w'T'}$ is the driving variable in the ASL over a slope, contrasting to the ASL over flat surfaces for which the driving variable is wind speed (Sun et al., 2012; Mahrt, 2014; Acevedo et al., 2016).
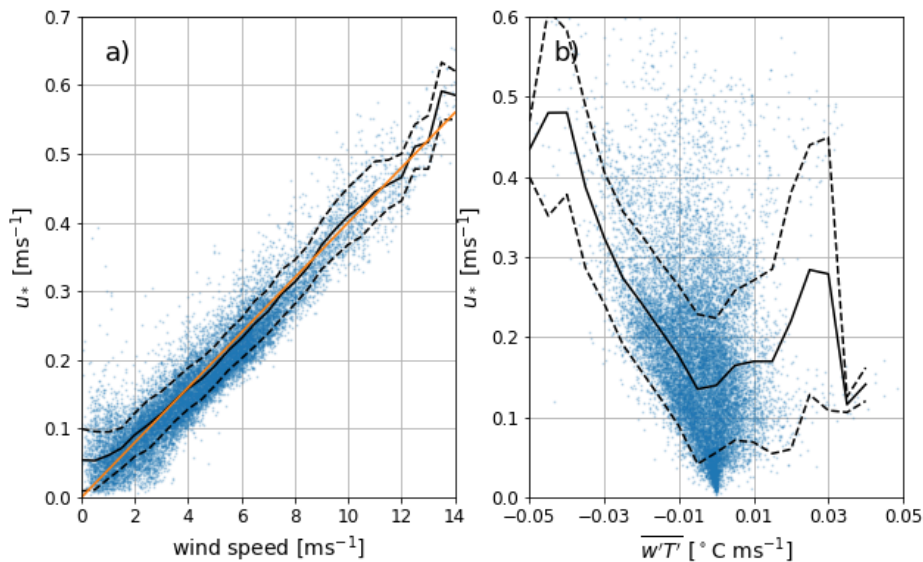

Figure 5.3: a) u_* as a function of wind speed. b) u_* as a function of $\overline{w'T'}$. The black line is the mean, the dashed is the mean $\pm$ SD, orange line is the theoretical curve $\overline{U} = 25u_*$.

5.2   The Validity of MOST

This section addresses of the validity of MOST in stable conditions as formulated through Equation 1.19. Equation 1.19 has been shown in previous studies to be valid for $\zeta < 0.1$ though extended by the validity of a local-scaling regime to $\zeta < 1$ (Grachev et al., 2005; Handorf et al., 1999). This result is not universal, Forrer and Rotach (1997) observed the validity to be $\zeta < 0.4$. With ζ greater than the critical value, the non-dimensional gradients level off. Physically this is an intuitive result as a strong vertical shear is unstable. Alternatively, large values of ζ can be due to errors in the calculation of u_* and therefore not physical. Figure 5.4 shows ϕ_M and ϕ_H for the F10, F14, and F18 campaigns. Equation 1.19 is valid for F10 and F14 until $\zeta = 0.2$ as predicted theoretically in Section 1.2. Equation 1.19 for this data set is valid for a shorter range of ζ values than for the data sets of Grachev et al. (2005), Handorf et al. (1999), and Forrer and Rotach (1997). The maximum stability regime due to katabatic flow may be responsible, as values of $\zeta > 0.2$ have a large scatter and do not occur often. Furthermore, the F18 campaign has longer lasting agreement with the theory as a result of having a 10% higher population for $\zeta \in [0.1, 1]$. For both F10 and F14, the non-dimensional gradient is underestimated, this is due to the underestimation of the local wind shear. F18 had better placement of the slow sensors and is in better agreement with the theory.
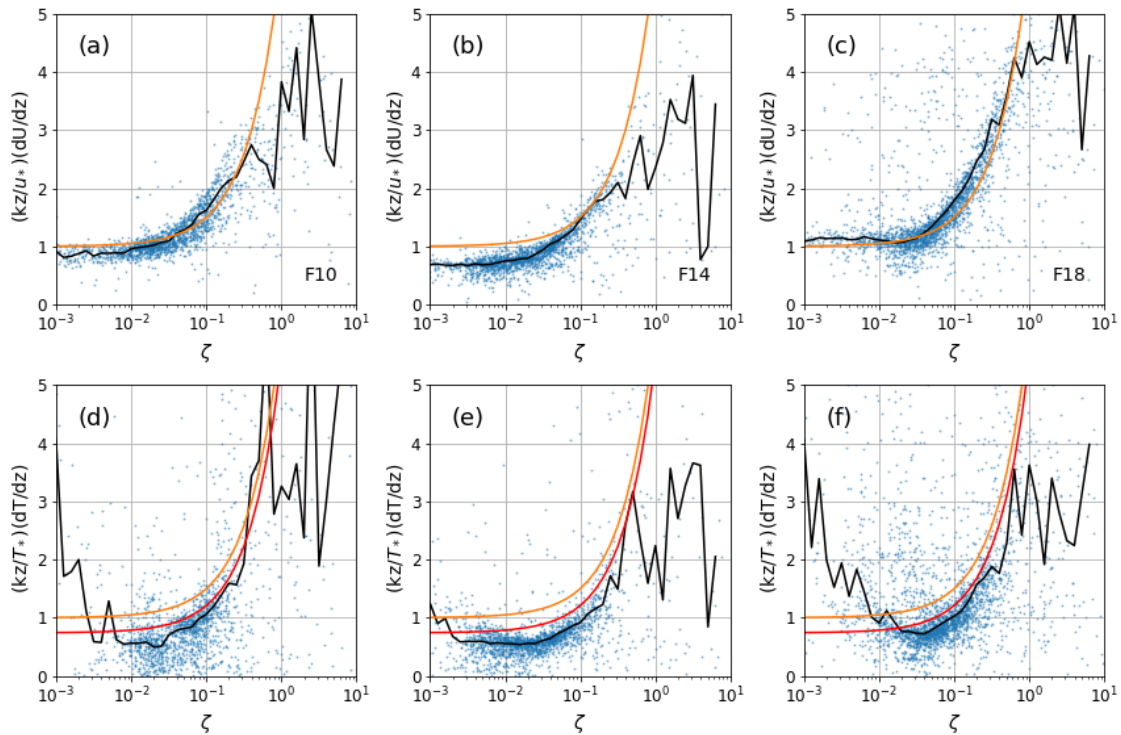
Figure 5.4: Non-dimensional gradients as a function of stability. The first row is ϕ_M for a) F10, b) F14, c) F18. The second is ϕ_H for d) F10, e) F14, f) F18. Equation 1.19 is plotted in orange, Equation 5.1 in red, and the median is plotted in black.

In contrast to ϕ_M, ϕ_H also has a lower bound of applicability at $\zeta = 10^{-2}$. From the observed scatter, the lower bound is most likely due to sensitivity in the calculations. Similar behaviour is seen in Handorf et al. (1999). In addition, ϕ_H is below Equation 1.19 for all

three campaigns. The red line is an alternative theoretical curve from Businger et al. (1971),

$$\phi_H(\zeta) = 0.74 + 4.7\zeta. \tag{5.1}$$

The better fit of Equation 5.1 to the data implies a $Pr_t < 1$. Direct calculation of Pr_t is not possible for the F10 and F14 campaigns without improving the methods for computing the vertical gradient. The error in the gradients will dominate the behaviour of Pr_t. For this reason, Pr_t as a function of ζ is only considered for the F18 campaign, plotted in Figure 5.5. There is a general decreasing trend of Pr_t with increasing stability. In $0.02 < \zeta < 0.2$, Pr_t is constant. This range is similar to the applicability of Equation 1.19 from Figure 5.4. This data suggests that for a gently stratified ASL, Pr_t is constant. This result is counter to Grachev et al. (2007) who observed a monotonically decreasing Pr_t with increasing stability.

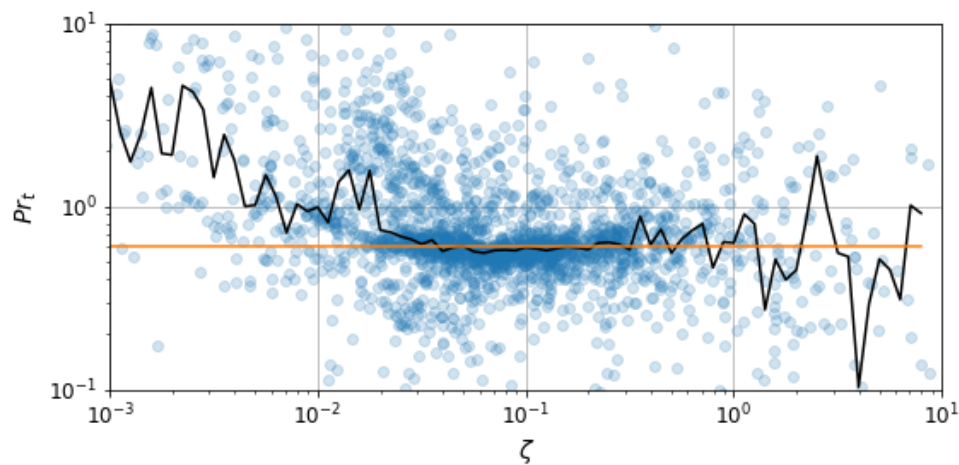*Figure 5.5: The Prantl number (Pr_t) as a function of ζ for the F18 data set. The black line is the median, and the orange line is $Pr_t = 0.6$.*

5.3 The Role of WM on MOST

As previously discussed, MOST is valid in homogeneous, steady states, where the local surface conditions control the ASL. The presence of waves will create non-local dependencies and introduce energy into the system on the same time-scale as the largest eddies. The time required for turbulence to adjust to the new energy source is not always rapid enough to maintain a quasi-steady state (Sun et al., 2015). It is them reasonable to guess that the presence of waves will alter the similarity relations discussed in Section 5.2. Following the WM approach of defining wave activity through the loop parameter (m), it is possible to concretely examine the influence of waves on MOST. For this purpose, the F18 data set was chosen due to its stability distribution. WM occurred in the F18 data set 28% of the time. Figure 5.6 shows the MOST relations for the full data set, cases with just WM, and cases with no WM. From looking at panels (b) and (e) from Figure 5.6, i.e the WM case, the similarity theory predicts the mean relatively well but extensive scatter is observed. Qualitatively it is difficult to ascertain relations from the figure. To quantify the differences, the standard deviation of the computed non-dimensional gradients for different stability classes is presented in Table 5.2. The largest standard deviations occur for the regions where MOST is not applicable or

computable, i.e $\zeta > 1$ for ϕ_M and ϕ_H, as well as $\zeta < 10^{-2}$ for ϕ_H. The *Corr.* columns show the percentage decrease in standard deviation by filtering out cases with wind meandering. For $10^{-1} < \zeta < 10^0$ the decrease is 16%, and 29% for ϕ_M, and ϕ_H respectively. This is the stability range with the strongest stratification for which the eddy-covariance is valid. The reduction in scatter, unfortunately, is not as large as hoped for and even without wave motions, a lot of scatter remains. The observed scatter is most likely due to the fixed averaging window which will misinterpret transient motions. Nonetheless, further investigation into using m to understand how waves affect the ASL is warranted following a similar approach. Improved flux calculation methods will increase the significance of the scatter removed through m, and new relationships may be observed.
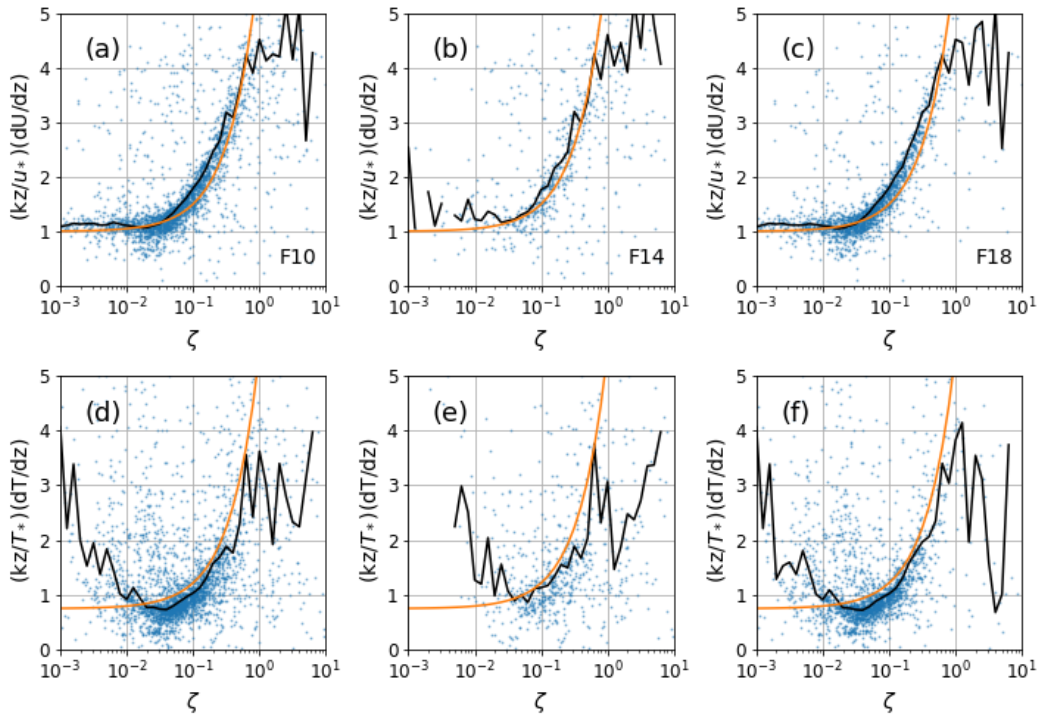

Figure 5.6: Non-dimensional gradients as a function of stability for the F18 data set. The first row is ϕ_M for a) the full data set, b) cases with WM, c) cases without WM. The second row is the same but for ϕ_H. Equation 1.19 is plotted in orange for ϕ_M, and Equation 5.1 for ϕ_H. The median is plotted in black.

Table 5.2: Standard deviation of vertical gradients for stability bins. Full is the full data set, WM is for cases with wind meandering, NM are cases with no wind meandering. The percent decrease in standard deviation between Full and NM is presented in Corr. .

	F18							
	ϕ_M				ϕ_H			
Stability Classes	Full	WM	NM	Corr.	Full	WM	NM	Corr.
$10^{-3} < \zeta < 10^{-2}$	0.61	0.77	0.58	5%	3.06	3.17	3.04	0.7%
$10^{-2} < \zeta < 10^{-1}$	0.68	1.01	0.58	15%	1.33	1.68	1.25	6%
$10^{-1} < \zeta < 10^0$	1.18	1.39	0.99	16%	1.92	2.45	1.35	29%
$10^0 < \zeta < 10^1$	2.34	2.35	2.31	1%	3.44	3.5	3.28	4.7%

Chapter 6

Conclusion and Outlook

In the hopes of improving the understanding of ASL in the polar regions, a new eddy covariance data set, *AA-MET-TURB*, was prepared and the potential of the data set was investigated. *AA-MET-TURB* is very promising for both Antarctic science and general meteorology.

Three Antarctica campaigns are included in *AA-MET-TURB* from the 2010-2011, 2014-2015, and 2018-2019 seasons. The data was collected at AWS5, a measurement site near Aboa station, Dronning Maud Land. AWS5 is located on a gently sloping glacier with a high level of horizontal homogeneity. The fetch from the mean wind direction is relatively undisturbed for over 100 km, making the site ideal for fundamental studies in boundary layer turbulence. The wind at AWS5 has remarkable directionally constancy, as both katabatic and synoptic forcing are climatologically from the east. AWS5 is in a similar katabatic zone as Halley station, and in a similar synoptic zone as Neumayer station. The mean wind speed, mean temperature, diurnal cycle, and albedo exhibits high variability between the different years. The ASL at AWS5 is therefore highly dependent on the presence and timing of synoptic systems travelling across the Weddell Sea. The 2018-2019 season had two storms stronger than the storms of the previous years. The estimated hourly-mean windspeed was 20 m/s, and persisted for up to three days. During the second storm, the geopotential height, for the 850 HPa level, which is normally around 1200 m cascaded to 1010 m.

To investigate oscillations in the eddy covariance data, the EAF of the streamline component of the wind was calculated for each hour interval. Using nonlinear regression, the EAFs were then projected onto Equation 4.2. The ratio between the timescale of decay and oscillation, m, can be used to distinguish signals which exhibit oscillatory behaviour. The distribution of m had a surprising bimodal structure, with a separation of scales around $m = 10^{-2}$. This allows for a strict criteria of $m > 10^{-2}$ for defining WM. This criteria was met for 34% of the intervals. WM was found to have no dependence on ζ, TKE, $\overline{w'T'}$ or wind direction. It was determined that WM can only occur when the 2 m wind speed is smaller than 8 m/s, and u_* is smaller than 0.4 m/s. When the ASL has high winds and strong surface stress, no waves can exist. At AWS5, the occurrence of WM has a diurnal cycle, which is even more significant if only persistent WM is considered. The maximum occurrence of persistent WM is between 20:00 and 23:00, with a secondary peak between 2:00 and 4:00. This is timed with the formation and dissipation of katabatic flows. Katabatic flows are the main mechanism for persistent WM at AWS5.

KFs were considered for cases where there are surface-based inversions. The criteria of $\Delta \overline{T} > 1°C$ was chosen, as to remove very weak KFs. Following this criteria, KFs occurred 27%, 17%, and 32% of 30 minute intervals, for the F10, F14, and F18 campaigns, respec-

tively. The KFs almost entirely come from the $60°$ - $120°$ sector. The highest occurrence of KFs is from 23:00 to 1:00, the period in between the maximums in occurrence of persistent WM. The behaviour of KFs is dependent on the strength and direction of the synoptic wind. The strongest KFs were observed to occur when the synoptic wind comes from the opposing direction. This counter-intuitive result can be explained by the accumulation of cold-air which is then released as a gravity current.

The behaviour of the ASL, due to the dynamics, is complicated. Analysis of the validity of MOST through Equation 1.19 is warranted. Before considering MOST, ζ was investigated. It was discovered that $\overline{w'T'}$ is the controlling parameter of the ASL on a slope. A decrease in $\overline{w'T'}$ will initially decreases u_* but then after $\overline{w'T'} = -0.05°Kms^{-1}$, u_* starts increasing. This can be deduced as $\overline{w'T'}$ forces katabatic wind which in turn increases u_*. As a result, the maximum stability occurs when $\overline{w'T'} = -0.05°Kms^{-1}$. In other words, the ASL on a slope has a maximum achievable ζ. Equation 1.19 was found to work for $\zeta < 0.2$. For the ϕ_H, Equation 5.1 is more appropriate as $Pr_t < 1$. For $0.02 < \zeta < 0.2$, the Pr_t number is constant at 0.6. In an attempt to improve the performance of Equation 1.19 and 5.1, the data set was filtered for values of $m > 10^{-2}$. This improved the $10^{-1} < \zeta < 10^0$ range by 16% and 29% for ϕ_M and ϕ_H, respectively.

As an aim of this thesis was also to discover interesting features and develop new research directions; I will end with a list of what I think are the five promising studies from *AA-MET-TURB*.

1. The variability observed between different seasons was found to be considerable. For that reason, a climatology of the synoptic systems in the eastern Weddell sea should be developed. This will contextualize the synoptic conditions of the 2010-2011, 2014-2015, and 2018-2019 seasons. How the different synoptic conditions influence the local meteorological conditions, and ASL turbulence, will provide a clear picture of the behaviour of the ASL over coastal Antarctic. Additionally, understanding how the synoptic conditions control the cloud-cover is also necessary to get the full picture.

2. Building on Chapter 5, an in depth investigation of the structure of turbulence is warranted. A novel location for eddy covariance observations with the advantage of the horizontal homogeneity should be taken advantage of. Validity of MOST, surface decoupling, instabilities in the slope flows, surface decoupling, all these topics should be brought together in one work.

3. Building on 1. , the synoptic conditions drive the local meteorology which is coupled to the snow surface. The albedo varies considerably between seasons. It is therefore dependent on the current synoptic conditions but also the synoptic history of the season. The ASL therefore has hysteresis through its coupling with the snow surface. The timing and strength of different systems can alter the snow conditions for the full austral summer. Connecting the meteorology and the snow physics would be very promising work.

4. In depth extension of the WM concept from low wind conditions to higher wind days. Most mechanism for oscillation in the wind are equally existent in high wind days,

therefore the wind speed does not discriminate the physics. Finding the bimodal structure implying a -yes- or -no- condition on oscillations is promising. That being said, proceeding should be done carefully. The methods should be developed fully before physicality is assumed.

5. The storms during the 2018-2019 campaign deserve further attention. Numerical modelling should be used to understand the formation, life, and dissipation of the storm. How did the storms intensify? Are these storms really stronger than the ones in previous years or is it just the lack of sampling? How does the occurrence of strong storms affect the snow surface?

Bibliography

Acevedo, O., Mahrt, L., Puhales, F., Costa, F., Medeiros, L., and Degrazia, G. (2016). Contrasting structures between the decoupled and coupled states of the stable boundary layer. *Quarterly Journal of the Royal Meteorological Society*, 142(695). 41

Anderson Jr., J. (2005). Ludwig Prandtl's Boundary Layer. *Physics Today*, (December). 3

Anfossi, D., Oettl, D., Degrazia, G., and Goulart, A. (2005). An analysis of sonic anemometer observations in low wind speed-conditions. *Boundary-Layer Meteorology*, pages 179–203. 2, 23, 24, 25

Atlaskin, E. and Vihma, T. (2012). Evaluation of NWP results for wintertime nocturnal boundary-layer temperatures over Europe and Finland. *Quarterly Journal of the Royal Meteorological Society*, 138(667):1440–1451. 1

Boe, J., Hall, A., and Qu, X. (2009). Comments on "current GCMs' unrealistic negative feedback in the arctic". *Journal of Climate*, 22. 1

Businger, J. A., Wyngaard, J. C., Izumi, Y., and Bradley, E. F. (1971). Flux-Profile Relationships in the Atmospheric Surface Layer. 6, 39, 43

Cava, D., Giostra, U., and Katul, G. (2015). Characteristics of Gravity Waves over an Antarctic Ice Sheet during an Austral Summer. *Atmosphere*, pages 1271–1289. 23

Cuxart, J., Holtslag, A. A., Beare, R. J., Bazile, E., Beljaars, A., Cheng, A., Conangla, L., Ek, M., Freedman, F., Hamdi, R., Kerstein, A., Kitagawa, H., Lenderink, G., Lewellen, D., Mailhot, J., Mauritsen, T., Perov, V., Schayes, G., Steeneveld, G. J., Svensson, G., Taylor, P., Weng, W., Wunsch, S., and Xu, K. M. (2006). Single-column model intercomparison for a stably stratified atmospheric boundary layer. *Boundary-Layer Meteorology*, 118(2):273–303. 1

Doran, J. and Horst, T. (1981). Velocity and Temperature Oscillations in Drainage Winds. 36

Dyer, A. (1974). A Review of Flux-Profile Relationships. *Boundary-Layer Meteorology*, 7:363–372. 6

Esau, I. and Zilitinkevich, S. (2010). On the role of the planetary boundary layer depth in the climate system. *Advances in Science and Research*, 4:63–69. 1

Fernando, H. and Weil, J. (2010). Whither the Stable Boundary Layer? A Shift in the Research Agenda. *Bulletin of the American Meteorological Society*. 1

Flores, O. and Riley, J. J. (2011). Analysis of Turbulence Collapse in the Stably Strati-fied Surface Layer Using Direct Numerical Simulation. *Boundary-Layer Meteorology*, 139(2):241–259. 1

Forrer, J. and Rotach, M. W. (1997). On the turbulence structure in the stable boundary layer over the Greenland ice sheet. *Boundary-Layer Meteorology*, 85(1):111–136. 12, 42

Goulart, A., Degrazia, G., Acevedo, O., and Anfossi, D. (2007). Theoretical considerations of meandering winds in simplified conditions. *Atmospheric Boundary Layers: Nature, Theory and Applications to Environmental Modelling and Security*, pages 123–131. 24, 29

Grachev, A. A., Andreas, E. L., Fairall, C. W., Guest, P. S., and Persson, P. O. G. (2007). SHEBA flux – profile relationships in the stable atmospheric boundary layer. *Boundary-Layer Meteorology*, pages 315–333. 6, 12, 43

Grachev, A. A., Fairall, C. W., Persson, P. O. G., Andreas, E. L., and Guest, P. S. (2005). Stable Boundary-Layer Scaling Regimes: The SHEBA data. *Boundary-Layer Meteorology*, pages 201–235. 6, 39, 42

Handorf, D., Foken, T., and Kottmeier, C. (1999). The stable atmospheric boundary layer over an Antarctic ice sheet. *Boundary-Layer Meteorology*, 91(2):165–189. 42

Hejstrup, J. (1993). A Statistical data screening procedure. *Measurement Science and Technology*. 9

Högström, U. (1988). Non-dimensional wind and temperature profiles in the atmospheric surface layer: A re-evaluation. *Boundary-Layer Meteorology*, 42(1-2):55–78. 6, 39

Högström, U. (1996). Review of some basic characteristics of the atmospheric surface layer. *Boundary-Layer Meteorology*, 78(January):215–246. 1, 4

Holmlund, P., Gjerde, K., Gundestrup, N., Hansson, M., Isaksson, E., Karlof, L., Nyman, M., Petterson, R., Pinglot, F., Reijmer, C. H., Stenberg, M., Thomassen, M., Van De Wal, R., Van Der Veen, C., Wilhelms, F., and Winther, J. G. (2000). Spatial gradients in snow layering and 10 m temperatures at two EPICA-Dronning Maud Land (Antarctica) pre-site-survey drill sites. *Annals of Glaciology*, 30:13–19. 14

Holtslag, A. A., Svensson, G., Baas, P., Basu, S., Beare, B., Beljaars, A. C., Bosveld, F. C., Cuxart, J., Lindvall, J., Steeneveld, G. J., Tjernström, M., and Van De Wiel, B. J. (2013). Stable atmospheric boundary layers and diurnal cycles: Challenges for weather and climate models. *Bulletin of the American Meteorological Society*, 94(11):1691–1706. 1, 2

Kärkäs, E. (2004). Meteorological Conditions of the Basen Nunatak in Western Dronning Maud Land, Antarctica, During the Years 1989-2001. *Geophysica*, 40:39–52. 19

Kilpeläinen, T. and Sjöblom, A. (2010). Momentum and Sensible Heat Exchange in an Ice-Free Arctic Fjord. *Boundary-Layer Meteorology*, 134(1):109–130. 10

König-Langlo, G., King, J. C., and Pettré, P. (1998). Climatology of the three coastal Antarctic stations Dumont d'Urville, Neumayer, and Halley. *Journal of Geophysical Research: Atmospheres*, 103(D9):10935–10946. 18, 20

Kouznetsov, R., Tisler, P., Palo, T., and Vihma, T. (2012). Evidence of Very Shallow Summertime Katabatic Flows in Dronning Maud Land, Antarctica. *Journal of Applied Meteorology and Climatology*, pages 164–168. 14, 34

Kral, S., Sjöblom, A., and Nygård, T. (2014). Observations of summer turbulent surface fluxes in a High Arctic fjord. *Quarterly Journal of the Royal Meteorological Society*, 140(679):666–675. 11, 12

Kral, S. T., Reuder, J., Vihma, T., Suomi, I., O'Connor, E., Kouznetsov, R., Wrenger, B., Rautenberg, A., Urbancic, G., Jonassen, M. O., Båserud, L., Maronga, B., Mayer, S., Lorenz, T., Holtslag, A. A., Steeneveld, G. J., Seidl, A., Müller, M., Lindenberg, C., Langohr, C., Voss, H., Bange, J., Hundhausen, M., Hilsheimer, P., and Schygulla, M. (2018). Innovative Strategies for Observations in the Arctic Atmospheric Boundary Layer (ISOBAR)-the Hailuoto 2017 campaign. *Atmosphere*, 9(7). 2, 13

Kundu, P. and Cohen, I. (2002). *Fluid mechanics, Second Edition*. 3

Lang, F., Belušić, D., and Siems, S. (2018). Observations of Wind-Direction Variability in the Nocturnal Boundary Layer. *Boundary-Layer Meteorology*, 166(1):51–68. 24

Mahrt, L. (1982). Momentum Balance of Gravity Flows. 23, 33, 38

Mahrt, L. (1989). Intermittency of Atmospheric Turbulence. *Journal of the Atmospheric Sciences*, 46(1):79–95. 2

Mahrt, L. (1998). Flux sampling errors for aircraft and towers. *Journal of Atmospheric and Oceanic Technology*, 15(2):416–429. 2

Mahrt, L. (2007). Weak-wind mesoscale meandering in the nocturnal boundary layer. *Environmental Fluid Mechanics*, 7(4):331–347. 2, 24

Mahrt, L. (2014). Stably Stratified Atmospheric Boundary Layers. *Annual Review of Fluid Mechanics*, 46(1):23–45. 10, 41

Mahrt, L. and Larsen, S. (1982). Small scale drainage front. *Tellus*, 34(6):578–587. 36

Mahrt, L., Richardson, S., Seaman, N., and Stauffer, D. (2012). Turbulence in the nocturnal boundary layer with light and variable winds. *Quarterly Journal of the Royal Meteorological Society*, (July):1430–1439. 23, 38

Mahrt, L., Sun, J., and Stauffer, D. (2015). Dependence of Turbulent Velocities on Wind Speed and Stratification. *Boundary-Layer Meteorology*, 155(1):55–71. 2, 6, 39

Mauder, M.; Foken, T. (2011). *Documentation and Instruction Manuel of the Eddy-Covariance Software Package TK3*. 7

Monin, A. S. and Obukhov, A. M. (1954). Basic laws of turbulent mixing in the surface layer of the atmosphere. *Contrib. Geophys. Inst. Acad. Sci. USSR*, 24(151):163–187. 3

Mortarini, L., Ferrero, E., Falabino, S., Trini Castelli, S., Richiardone, R., and Anfossi, D. (2013). Low-frequency processes and turbulence structure in a perturbed boundary layer. *Quarterly Journal of the Royal Meteorological Society*, 139(673):1059–1072. 2, 25

Mortarini, L., Maldaner, S., Moor, L. P., Stefanello, M. B., Acevedo, O. C., Degrazia, G., and Anfossi, D. (2016a). Temperature auto-correlation and spectra functions in low-wind meandering conditions. *Quarterly Journal of the Royal Meteorological Society*, (July):1881–1889. 32

Mortarini, L., Stefanello, M., Degrazia, G., Roberti, D., Castelli, S. T., and Anfossi, D. (2016b). Characterization of Wind Meandering in Low-Wind-Speed Conditions. *Boundary-Layer Meteorology*, 161(1):165–182. 25, 28

Nygård, T., Tisler, P., Vihma, T., Pirazzini, R., Palo, T., and Kouznetsov, R. (2017). Properties and temporal variability of summertime temperature inversions over Dronning Maud Land, Antarctica. *Quarterly Journal of the Royal Meteorological Society*, 143(702):582–595. 10

Oettl, D., Goulart, A., Degrazia, G., and Anfossi, D. (2005). A new hypothesis on meandering atmospheric flows in low wind speed conditions. *Atmospheric Environment*, 39(9):1739–1748. 24, 25

Parish, T. and Bromwich, D. (1997). On the forcing of seasonal changes in surface pressure over Antarctica. *Journal of Geophysical Research*, 102(D12):13785–13792. 33

Parish, T. R. (1982). Surface Airflow Over East Antarctica. *Monthly Weather Review*. 33

Parish, T. R. and Bromwich, D. H. (1998). A Case Study of Antarctic Katabatic Wind Interaction with Large-Scale Forcing*. *Monthly Weather Review*, 126(1):199–209. 33

Parish, T. R. and Cassano, J. J. (2003). The Role of Katabatic Winds on the Antarctic Surface Wind Regime. *Monthly Weather Review*, 131(2):317–333. 33

Parish, T. R. and Waight, K. T. (1987). The Forcing of Antarctic Katabatic Winds. 33

Periard, C. and Pettre, P. (1993). Some aspects of the climatology of Dumont d'Urville, Adelie Land, Antarctica. *International Journal of Climatology*, (313). 33

Pirazzini, R. (2004). Surface albedo measurements over Antarctic sites in summer. *Journal of Geophysical Research D: Atmospheres*, 109(20):1–15. 21

Rees, J., Denholm-Price, J., King, J., and Anderson, P. (2000). A climatological study of internal gravity waves in the atmospheric boundary layer overlying the Brunt Ice Shelf, Antarctica. *Journal of the Atmospheric Sciences*, 57:511–526. 23

Reijmer, C. H. and Oerlemans, J. (2002). Temporal and spatial variability of the surface energy balance in Dronning Maud Land, East Antarctica. *Journal of Geophysical Research Atmospheres*, 107(24). 18

Savijärvi, H. (2011). Antarctic local wind dynamics and polynya effects on the Adélie Land coast. *Quarterly Journal of the Royal Meteorological Society*, 137(660):1804–1811. 33

Schotanus, P., Nieuwstadt, F. T., and De Bruin, H. A. (1983). Temperature measurement with a sonic anemometer and its application to heat and moisture fluxes. *Boundary-Layer Meteorology*, 26(1):81–93. 10

Sjöblom, A. (2003). The turbulent kinetic energy budget in the marine atmospheric surface layer. *Journal of Geophysical Research*, 107(C10):1–18. 10

Sjöblom, A. (2014). Turbulent fluxes of momentum and heat over land in the High-Arctic summer: The influence of observation techniques. *Polar Research*, 33(1 SUPPL). 10

Smedman, A., Tjernström, M., and Högström, U. (1993). Analysis of the Turbulence Structure of a Marine Low-Level Jet. *Boundary-Layer Meteorology*, 66:105–126. 1

Streten, N. (1990). A review of the climate of Mawson - a representative strong wind site in East Antarctica. *Antarctic Science*, 2(7):79–89. 33

Sun, J., Burns, S. P., Lenschow, D. H., Banta, R., Newsom, R., Coulter, R., Frasier, S., Ince, T., Nappo, C., Cuxart, J., Blumen, W., Lee, X., and Hu, X.-Z. (2002). Intermittent turbulence associated with a density current passage in the stable boundary layer. *Boundary-Layer Meteorology*, pages 199–219. 2

Sun, J., Lenschow, D. H., Burns, S. P., Banta, R. M., Newsom, R. K., Coulter, R., Frasier, S., Ince, T., Nappo, C. J., Mahrt, L., Miller, D., and Skelly, B. (2004). Atmospheric disturbances that generate intermittent turbulence in Nocturnal Boundary Layers. *Boundary-Layer Meteorology*, 110:255–279. 2

Sun, J., Mahrt, L., Banta, R. M., and Pichugina, Y. L. (2012). Turbulence Regimes and Turbulence Intermittency in the Stable Boundary Layer during CASES-99. *Journal of the Atmospheric Sciences*, pages 338–351. 38, 39, 41

Sun, J., Mahrt, L., Nappo, C., and Lenschow, D. H. (2014). Wind and Temperature Oscillations Generated by Wave – Turbulence Interactions in the Stably Stratified Boundary Layer. *Journal of Atmospheric Sciences*, pages 1484–1503. 2

Sun, J., Nappo, C. J., Mahrt, L., Belušic, D., Grisogono, B., Stauffer, D. R., Pulido, M., Staquet, C., Jiang, Q., Pouquet, A., Yagüe, C., Galperin, B., Smith, R. B., Finnigan, J. J., Mayor, S. D., Svensson, G., Grachev, A. A., and Neff, W. D. (2015). Review of wave-turbulence interactions in the stable atmospheric boundary layer. *Reviews of Geophysics*, 53(3):956–993. 2, 43

Suomi, I., Gryning, S.-E., O'Connor, E. J., and Vihma, T. (2017). Methodology for obtaining wind gusts using Doppler lidar. *Quarterly Journal of the Royal Meteorological Society*, (July):2061–2072. 9

Troen, I. and Lundtang Petersen, E. (2012). *European Wind Atlas*. 20

Valkonen, T., Vihma, T., Kirkwood, S., and Johansson, M. (2010). Fine-scale model simulation of gravity waves generated by Basen nunatak in Antarctica. *Tellus, Series A: Dynamic Meteorology and Oceanography*, 62(3):319–332. 14

van de Wiel, B., Moene, A. F., Steeneveld, G. J., Hartogensis, O. K., and Holtslag, A. A. M. (2007). Predicting the Collapse of Turbulence in Stably Stratified Boundary Layers. *Flow Turbulence Combust*, pages 251–274. 1

Van de Wiel, B. J. H., Moene, A., Hartogenesis, O., De Bruin, H., and Holtslag, A. A. M. (2003). Intermittent Turbulence in the Stable Boundary Layer over Land . Part III : A Classification for Observations during CASES-99. *Journal of Atmospheric Sciences*, pages 2509–2522. 2

Van de Wiel, B. J. H., Moene, A., Ronda, R. J., De Bruin, H., and Holtslag, A. A. M. (2002a). Intermittent Turbulence and Oscillations in the Stable Boundary Layer over Land . Part II : A System Dynamics Approach. *Journal of Atmospheric Sciences*, pages 2567–2581. 2

Van de Wiel, B. J. H., Ronda, R. J., Moene, A. F., De Bruin, H., and Holtslag, A. A. M. (2002b). Intermittent Turbulence and Oscillations in the Stable Boundary Layer over Land . Part I : A Bulk Model. *Journal of the Atmospheric Sciences*, pages 942–958. 2

Van den Broeke, M., Reijmer, C., Van As, D., and Boot, W. (2006). Daily cycle of the surface energy balance in Antarctica and the influence of clouds. *International Journal of Climatology*, 26(12):1587–1605. 18

van den Broeke, M., Winther, J.-g., Isaksson, E., Pinglot, J. F., Karlöf, L., Eiken, T., and Conrads, L. (1999). Climate variables along a traverse line in Dronning Maud Land, East Antarctica. *Journal of Glaciology*, 45(150):295–302. 14

Van den Broeke, M. R., Reijmer, C., Van As, D., Van de Wal, R., and Oerlemans, J. (2005). Seasonal cycles of Antarctic surface energy balance from automatic weather stations. *Annals of Glaciology*, 41(Aws 4):131–139. 13, 14

Vickers, D., Mahrt, L., and Belušić, D. (2008). Particle simulations of dispersion using observed meandering and turbulence. *Acta Geophysica*, 56(1):234–256. 24

Vihma, T., Pirazzini, R., Fer, I., Renfrew, I., Sedlar, J., Tjernström, M., Lüpkes, C., Nygård, T., Notz, D., Weiss, J., Marsan, D., Cheng, B., Birnbaum, G., Gerland, S., Chechin, D., and Gascard, J. (2014). Advances in understanding and parameterization of small-scale physical processes in the marine Arctic climate system: A review. 1, 2

Vihma, T., Tuovinen, E., and Savijrvi, H. (2011). Interaction of katabatic winds and near-surface temperatures in the Antarctic. *Journal of Geophysical Research Atmospheres*, 116(21):1–14. 33

Weibull, W. (1951). A Statistical Distribution Function of Wide Applicability. *Journal of Applied Mechanics*, 18:293–297. 19

Wendler, G., Stearns, C., Weidner, G., Dargaud, G., and Parish, T. (2004). On the extraordinary katabatic winds of Adélie Land. *Journal of Geophysical Research: Atmospheres*, 102(D4):4463–4474. 32

Wilczak, J., Oncley, S., and Stage, S. (2001). Sonic anemometer tilt correction algorithms. *Boundary-Layer Meteorology*, 99(1):127–150. 11